Final Report on the OFES ELM Milestone for FY2006

September 30, 2006

D. C. Barnes[1], J. Breslau[2], R. A. Bayliss[3], D. P. Brennan[4,5], E. D. Held[6], S. C. Jardin[2 †], S. E. Kruger[7], A. Y. Pankin[8], D. D. Schnack[3], C. R. Sovinec[3], H. R. Strauss[9], L. Sugiyama[10], and the NIMROD and M3D Teams

[1]University of Colorado, Boulder, Colorado
[2]Princeton Plasma Physics Laboratory
[3]University of Wisconsin, Madison, Wisconsin
[4]University of Tulsa, Tulsa, Oklahoma
[5]General Atomics, San Diego, California
[6]Utah State University, Logan, Utah
[7]Tech-X Corporation, Boulder, Colorado
[8]Lehigh University, Bethlehem, Pennsylvania
[9]New York University, New York, New York
[10]Massachusetts Institute of Technology, Cambridge, Massachusetts

[†] Editor for the SciDAC Center for Extended Magnetohydrodynamics (CEMM)

Full Legal Disclaimer

Trademark Disclaimer

Executive Summary

This document reports the successful completion of the OFES Theory Milestone for FY2006: *Increase resolution in simulations of macroscopic plasma edge phenomena. Optimizing confinement and predicting the behavior of burning plasmas require improved simulations of edge and core plasma phenomena, as the characteristics of the edge can strongly affect core confinement. For this quarterly milestone, we will simulate nonlinear plasma edge phenomena using extended MHD codes with a resolution of 40 toroidal modes.*

An important issue for fusion plasma theory is the occurrence of Edge Localized Modes (ELMs) in tokamak plasmas. We apply large-scale numerical computation with fluid-based plasma models to ELM-unstable equilibrium profiles that have been fit to data from the DIII-D device at General Atomics (http://fusion.gat.com/diii-d/). Building upon the successful completion of the milestone for FY2005, we include the number density profile created from laboratory observations and electron-fluid dynamics, in addition to increased spatial resolution for the toroidal coordinate and the poloidal plane. The effects of toroidal ion flow are considered through computations with resistive magnetohydrodynamics (MHD).

The linear and nonlinear ELM computations are performed with both the NIMROD (http://nimrodteam.org) and M3D (http://w3.pppl.gov/~jchen/) codes. These each allow users to select from MHD and two-fluid models. The Hall and electron pressure terms distinguish the two-fluid electric field, as appropriate for low-frequency dynamics. The present two-fluid models also include the Braginskii gyroviscous stress in the ion evolution. Many of the computations include anisotropic thermal conduction. For the NIMROD code, the ratio of parallel and perpendicular thermal conductivities is 10^7 in the 40-mode nonlinear two-fluid computation. The M3D code uses the "artificial sound wave" method to simulate high thermal conductivity in a computationally efficient way. These computations also have temperature-dependent electrical resistivity computed locally from the evolving three-dimensional temperature profile.

Linear calculations for an equilibrium that is fit to measurements of DIII-D discharge 113317 test the numerical convergence properties of the present NIMROD algorithm on ELMs. Substantial poloidal resolution is required to reproduce eigenfunctions with large toroidal wave numbers (n), but the radial resolution can be economized provided that the computational mesh is packed near the separatrix of the equilibrium. Convergence is then established with finite element basis functions of polynomial degree as large as 7 for MHD modeling and 8 for two-fluid modeling. The resistive MHD calculations find growth-rates that increase with n, but the two-fluid model shows a cutoff for $n \geq 30$. The radial profile of the diamagnetic drift is narrower than the width of the intermediate-n modes, and the stabilization is not as strong as the Roberts-Taylor result for slab geometry. This is consistent with the M3D result that for a given n mode, stabilization will occur if the two fluid parameter H is sufficiently large.

In the NIMROD nonlinear two-fluid computation, coupling among the unstable band of modes at intermediate n-values generates harmonics in the linearly stable range of wave numbers that are evolved ($n \leq 42$). The nonlinear coupling also produces an n=1 distortion. The unstable modes are resonant at or near the q=3 surface, so the n=1 distortion induces an m=3 pattern in poloidal angle. This collects fine-scale spatial oscillations into a localized helical structure as the perturbation amplitude approaches the level of the density and temperature pedestal of the equilibrium. Nonlinear MHD modeling shows that toroidal flow does not allow large temperature perturbations to extend to the wall, as occurs without flow.

The M3D two-fluid calculation utilized extreme radial and poloidal grid packing as required for toroidal mode number n=0,...,40. Special techniques had to be developed to deal with the large density gradients to keep the density from going negative. A significant result is that temperature perturbations are much less than the density perturbations during the nonlinear phase, in apparent agreement with experimental observations. Plasma is able to cross from closed magnetic field lines inside the magnetic separatrix to open field lines outside the magnetic separatrix. When three dimensional magnetic perturbations are present, the magnetic separatrix becomes ill defined, stochastically connecting regions of closed and open magnetic field lines.

I. Introduction

The confinement achieved in present-day tokamak plasmas largely results from the transport barrier that forms just inside the separatrix of the equilibrium magnetic field. However, free energy associated with large pressure and current gradients in this region is prone to excite Edge Localized Modes (ELMs) that release some of the stored internal energy in discrete bursts. While the ELMs may be viewed as a self-regulating mechanism of the plasma, the projected amount of released energy for certain classes of ELM events in a device the size of ITER raises concern for the longevity of structural components. As such, ELMs are identified in the 2002 Fusion Summer Study (http://fire.pppl.gov/snowmass02_report.pdf) as one of the critical magnetohydrodynamics (MHD) theory topics for assessing burning plasma designs, and they remain an area of central importance for fusion theory.

There have been significant advances in our understanding of the linear properties of ELMs [1-2], but their nonlinear evolution is a largely unexplored topic for theoretical modeling. An early nonlinear study solves compressible reduced-MHD equations in a global geometry with the core-plasma region removed [3]. The equilibrium generated in the computation excites ballooning instabilities at low toroidal mode index (n) that drive poloidal flows into the divertor late in the nonlinear stage. A more recent study applies a reduced two-fluid model to selected toroidal harmonics in a narrow region around the separatrix [4] and finds a toroidally localized structure emerging late in the evolution. The localization represents nonlinear coupling of multiple unstable modes and is consistent (in the context of the selected harmonics) with laboratory observations of filamentary structures. Even with this progress, there remain open theoretical questions regarding modal coupling with a full spectrum, the impact on the global profile, the recovery cycle, and how externally controllable parameters may influence the ELM activity. In the near term, we expect to be able to apply large-scale nonlinear simulation to ELM activity in isolation or with limited interaction with core MHD dynamics. In the longer term, predictive integrated modeling must incorporate ELM dynamics as one part of a self-consistent numerical description of a magnetically confined, burning plasma.

In this report we describe two studies of the nonlinear evolution an ELM event using two different 3D Extended MHD codes, NIMROD and M3D. Although the studies are addressing the same initial equilibrium, many of the details of the underlying mathematical model, the initial and boundary conditions differ. This is meant to be an exploratory study in which we show that these codes are capable of predicting ELM behavior, and in so doing are able to reproduce many experimental observations. However, this limited study does not claim to provide a benchmark between the two codes, nor does it claim to be a definitive study of the nonlinear evolution of ELMs.

In Part II we present a detailed description of the NIMROD study of ELMs. This is followed in Part III with a description of the M3D study of ELMs, concentrating on recent high-resolution nonlinear calculations. We conclude in Part IV with a summary of the main physics results and the outlook for further progress.

II. Computational Studies with the NIMROD Code

1. Preliminaries

This section describes recent nonlinear studies of ELMs with the NIMROD code[7]. The computational domain includes the full core region and a large edge-plasma region. The equilibria are pre-computed numerical solutions [5] to the Grad-Shafranov equation with profiles fitted to laboratory measurements of ELM-producing discharges in the DIII-D tokamak at General Atomics [6]. Linear and nonlinear computations with a broad range of toroidal components ($0 \le n \le 42$) are performed with the non-ideal MHD model and with the two-fluid model. The linear computations verify the stabilizing effect of two-fluid physics on modes of large toroidal wave-number, as expected from ballooning-mode analysis [8]. In addition, our largest nonlinear two-fluid simulation finds nonlinear coupling generating the localization anticipated from the earlier selected-harmonic computation [4].

Numerically, the ELM computations have properties that are distinct from more traditional applications of NIMROD, which focus on magnetic-tearing and internal (to the plasma) kink activity [9]. Besides the interchange-like nature of ELMs, the broad unstable band at relatively large wavenumber requires new levels of spatial-scale variation in each computation. A simple statement of increased toroidal resolution belies the corresponding increase of poloidal resolution needed to capture field-line resonance near the separatrix and the impact on the condition numbers of large matrices that are solved at each step of the temporal advance.

The organization for this section describing the NIMROD studies is as follows: the fluid models and equilibrium profile information are described in Sect. 2, linear stability and numerical convergence are described in Sect. 3, algorithm development for the nonlinear two-fluid computation is discussed in Sect. 4, and nonlinear MHD and two-fluid results are presented in Sect. 5. Our conclusions in Sect. 6 highlight the implications of algorithmic and computing performance encountered during the course of this effort.

2. Fluid models and equilibria

Our numerical computations solve single- and two-fluid models of macroscopic plasma dynamics. The former is essentially MHD extended to include anisotropic thermal transport. The latter is expressed in single-fluid form [10] and does not consider electron inertia, which is important only at high frequency or in conditions of 'collisionless' magnetic tearing. In addition, electron stress, which plays a critical role in neoclassical physics, has not yet been included, and the single-temperature modeling considered here assumes rapid thermal equilibration among the electron and ion species for convenience. The equations are

$$\frac{\partial \mathbf{B}}{\partial t} = -\nabla \times \mathbf{E} + \kappa_{divb} \nabla \nabla \cdot \mathbf{B} \tag{1}$$

$$\mu_0 \mathbf{J} = \nabla \times \mathbf{B} \tag{2}$$

$$\frac{\partial n}{\partial t} + \nabla \cdot (n\mathbf{V}) = \nabla \cdot (D \nabla n) \tag{3}$$

$$\rho \left(\frac{\partial \mathbf{V}}{\partial t} + \mathbf{V} \cdot \nabla \mathbf{V} \right) = \mathbf{J} \times \mathbf{B} - \nabla p - \nabla \cdot \Pi_i \tag{4}$$

$$\frac{3n}{2}\left(\frac{\partial T}{\partial t}+\mathbf{V}\cdot\nabla T\right)=-nT\,\nabla\cdot\mathbf{V}+\nabla\cdot\left\{n\left[\left(\chi_{\parallel}-\chi_{\perp}\right)\hat{\mathbf{b}}\hat{\mathbf{b}}+\chi_{\perp}\mathbf{I}\right]\cdot\nabla T\right\} \tag{5}$$

where n is the electron number density, ρ is the mass density ($m_i n$ for single charged ions), T is temperature (multiplied by the Boltzmann constant), p is the sum of electron and ion pressures ($2nT$), **V** is the center-of-mass flow velocity, **B** is magnetic induction, and **J** is charge-current density. Heating terms have been omitted from the temperature evolution with the expectation that they are negligible during the rapid growth of an ELM. However, large thermal diffusivity ($\chi_{\parallel}$) parallel to the direction ($\hat{\mathbf{b}}$) of the magnetic field can affect heat flow, so thermal conduction is included. The second term on the right side of Eq. (1) is numerical and is used to control magnetic divergence error [7]. The term on the right side of (3) is also numerical and is used to stabilize the number density representation. (See Sections 3 and 4.)

Our single- and two-fluid models are distinguished by the relations used for the electric field (**E**) and the ion stress tensor (Π_i). For single-fluid (resistive MHD),

$$\mathbf{E}=\eta\,\mathbf{J}-\mathbf{V}\times\mathbf{B} \tag{6}$$

in Eq. (1), whereas the electric field used in our two-fluid ELM computations is

$$\mathbf{E}=\eta\,\mathbf{J}-\mathbf{V}\times\mathbf{B}+\frac{1}{ne}\mathbf{J}\times\mathbf{B}-\frac{T}{ne}\nabla n \quad . \tag{7}$$

The purely electrostatic contribution ($\sim\nabla T$) from the electron pressure cannot influence the evolution of the magnetic field and is omitted. Plasma kinetics shows that electrical resistivity (η) depends on temperature as $T^{-3/2}$ [11]. The nonlinear NIMROD MHD computations performed for the FY2005 milestone [12] computed the evolving resistivity profile using the toroidally averaged temperature, but the two-fluid simulation discussed in Sect. 5 uses the local temperature for full three-dimensional spatial variation of resistivity. To assist numerical convergence, however, the magnitude of the resistivity profile is scaled—see Sect. 3. The ion stress tensor in both models includes viscous damping ($\rho\nu\mathbf{W}$, where ν is the viscous diffusivity) that is proportional to the traceless rate-of-strain tensor,

$$\mathbf{W}\equiv\nabla\mathbf{V}+\left(\nabla\mathbf{V}\right)^{T}-\frac{2}{3}\mathbf{I}\left(\nabla\cdot\mathbf{V}\right)$$

where **I** is the identity tensor. Our two-fluid modeling also includes the Braginskii gyroviscous stress [13]

$$\Pi_{gv}=\frac{m_i nT}{4eB}\left[\hat{\mathbf{b}}\times\mathbf{W}\cdot\left(\mathbf{I}+3\hat{\mathbf{b}}\hat{\mathbf{b}}\right)-\left(\mathbf{I}+3\hat{\mathbf{b}}\hat{\mathbf{b}}\right)\cdot\mathbf{W}\times\hat{\mathbf{b}}\right] \tag{8}$$

that is derived under the assumption of $\mathbf{E}\times\mathbf{B}$ drift motion being comparable to thermal speeds. This condition is not realized in tokamak plasmas (fortunately), but including Braginskii gyroviscous stress is a significant step toward an accurate representation of magnetization flow effects in the momentum evolution equation.

In many cases, tokamak MHD activity produces small perturbations to the large background magnetic field, density, pressure, etc., so the typical application of NIMROD decomposes each physical field into a time-dependent perturbation and a steady background (or equilibrium) part. Analyzing a particular configuration is then accomplished by using the relevant profile as the

steady background. [The numerical sources described in the milestone report for the first quarter of FY2006[‡] provide an alternative treatment, where the large background is not separate but needs to be driven.] In the computations described below, we use MHD equilibria fitted to experimental data from the DIII-D discharges numbered 113207 and 113317. The magnetic flux distribution for the fit of 113317 is shown in Fig. II.1, and flux-surface quantity profiles are shown in Fig. II.2. Unlike the computations described in the FY2005 milestone report, which have a uniform particle number density profile, the present computations use density profiles that are based on laboratory measurements. Both the temperature profile and the number density profile drop by approximately a factor of four from just inside to outside the separatrix. To simplify the edge plasma region, it is considered to have uniform temperature and number density at the values provided by the equilibrium file for the separatrix (100 eV and 1.2×10^{19} m^{-3}, respectively, for the 113317 discharge).

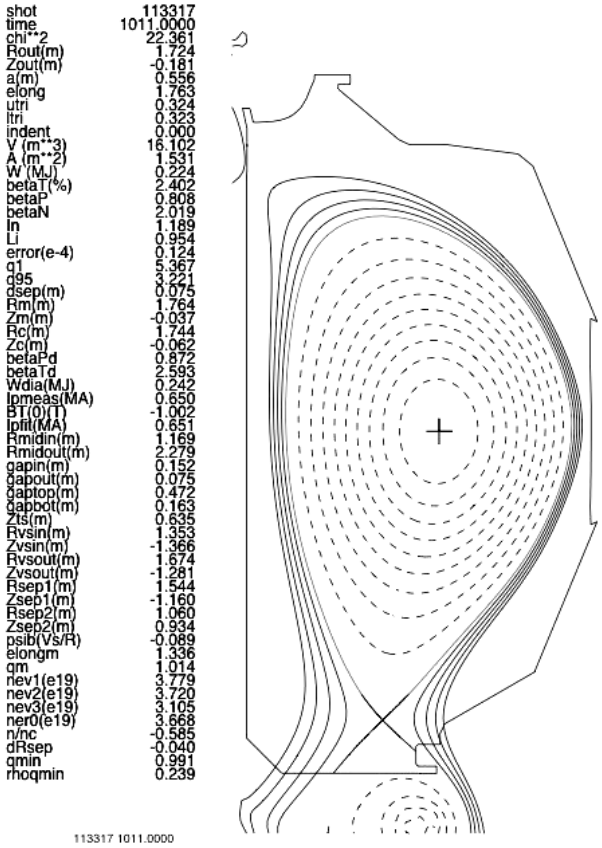

Figure II.1. Magnetic flux distribution and parameters for the equilibrium fitted to DIII-D discharge 113317 with the EFIT code [5].

[‡] Available from http://w3.pppl.gov/cemm/Milestones/elm_milestone_06Q1R-3.pdf .

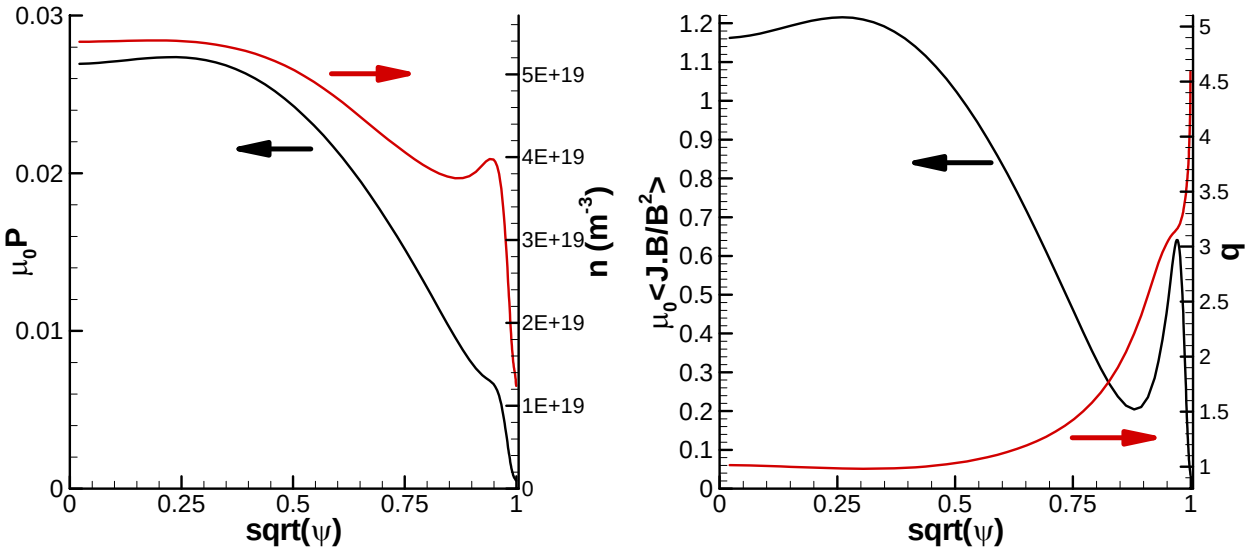

Figure II.2. Flux-surface profiles for the equilibrium fit to discharge 113317. Equilibrium pressure and number density are shown on the left, and average parallel current density and safety factor are shown on the right. This particular fit of 113317, numbered 3450_k1.4, is a slight adjustment (courtesy of Dr. Phillip Snyder, General Atomics) of what is shown in Fig. II.1. Linear calculations presented in Sect. 3 and two-fluid computations in Sect. 5 use this fit.

3. Linear Convergence

With their broad range of unstable toroidal mode numbers of order 10 and radial localization to regions where the *q*-value increases sharply, ELMs tend to have high poloidal mode numbers (m). The radial localization coincides with the pressure and current density gradients that drive the modes. The implications for spatial resolution requirements in numerical computations is unlike most other applications of global MHD simulation, and it is therefore important to test convergence properties—linearly as a start but ultimately nonlinearly as well. We have performed numerous linear calculations with the 113317 equilibrium profiles shown in Fig. II.2. The NIMROD code uses high-order quadrilateral finite elements for the poloidal plane, and finite Fourier series for the toroidal direction. The order of the polynomial basis functions may be varied, and for these computations, we find it advantageous to pack the elements radially near the separatrix, leaving the core with relatively large elements, as shown in Fig. II.3. The mesh is well aligned with the equilibrium magnetic flux except near the *X*-point and in the open-field region. The boundary of the domain conforms to the shape of the closed flux surfaces and is located at approximately the same average distance from the separatrix as the wall in the experiment (compare with Fig. II.1). Linear computations on similar meshes have been performed with the order of the polynomial bases varied from two (biquadratic elements) to eight.

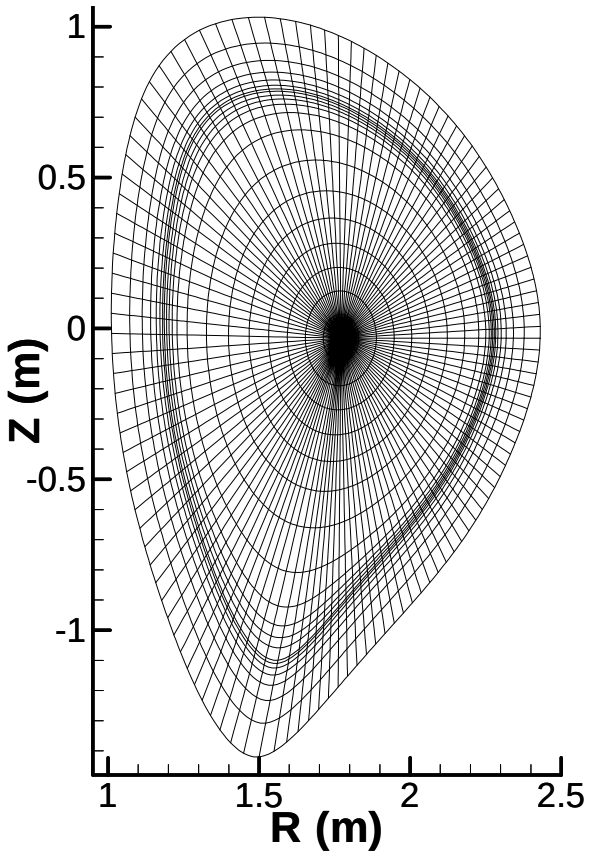

Figure II.3. Mesh of typical curved quadrilateral elements used in linear and nonlinear ELM computations. The resolution in this example is 20×120 (radial×azimuthal), and the mapping to physical coordinates is C^0 bicubic.

Linear calculations have been performed for both single- and two-fluid models with a range of physical and numerical parameters. Ultimately, physical parameters will be determined by the plasma conditions in the experiment, but the non-dissipative nature of the NIMROD algorithm [7] often leads to noisy solutions when physical damping is not present, hence the need for the artificial particle diffusivity in Eq. (3), for example. Dissipation is also a factor in the advance of magnetic field. For example, one sequence of single-fluid calculations for the n=13 mode with realistic values of resistive diffusivity ($\eta/\mu_0 \cong 0.07$ m^2/s in the pedestal region), $\chi_{\|}$=3.75×10^6 m^2/s, $\chi_{\perp}$=37.5 m^2/s, and D=25 m^2/s does not show convergence with respect to poloidal mesh resolution for bicubic elements. With 28 elements in the radial direction and 72, 144, and 288 elements in the poloidal angle, the growth rates of the resulting numerical eigenmodes are 3.7×10^5, 1.9×10^5, and 5.7×10^4 s^{-1}, respectively. [The toroidal Alfvén propagation time ($\tau_A \equiv R_0\sqrt{\mu_0\rho_0}\,/B_0$) is 8.52×10^{-7} s.] However, we are able to demonstrate convergence when the temperature-dependent resistivity profile is multiplied by a factor that brings the resistive diffusivity in the pedestal to 7 m^2/s, even when the artificial particle diffusivity is reduced to 2.5 m^2/s. Figure II.4 shows growth rates from several sequences of computations with isotropic thermal diffusivity. The two sequences with more than 100 elements in the poloidal angle show convergence for polynomials of degree larger than 5. The magnetic divergence error (Fig. II.5) also confirms convergence for the larger-degree polynomials.

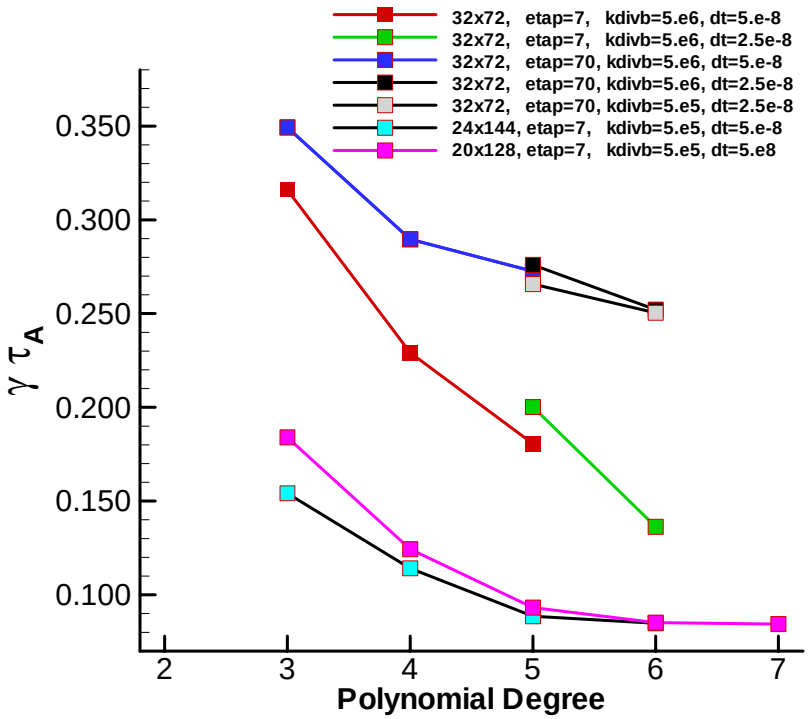

Figure II.4. Numerical convergence studies with respect to the degree of the polynomial basis functions for the MHD model with isotropic thermal diffusivity of 300 m^2/s and ν=25 m^2/s. The mesh and pedestal electrical diffusivity ("etap"), magnetic divergence cleaning diffusivity (κ_{divb}), and time-step values for each sequence are indicated in the legend.

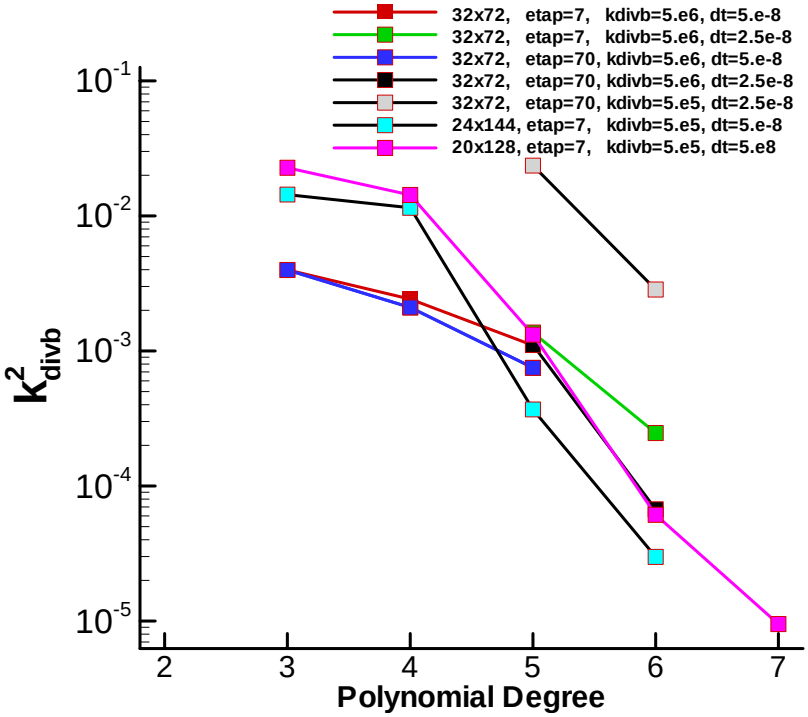

Figure II.5. Magnetic divergence error, measured as $\int\left(\nabla\cdot\tilde{b}\right)^2 dVol \Big/ \int\tilde{b}^2 dVol$ for the same numerical sequences shown in Fig. II.4.

Similar convergence tests have been performed for other toroidal components with isotropic and anisotropic ($\chi_{\parallel}$=1.5×10^{7} m^{2}/s, $\chi_{\perp}$=1.5 m^{2}/s) thermal conduction. Figure II.6 shows that the MHD modes with larger n-values require more poloidal resolution to achieve convergence, as expected from the resonance condition of m=*q*n. The finer poloidal structure of the n=42 mode relative to the n=13 is evident from the computed eigenfunctions (Fig. II.7). The larger n-value modes also have larger growth rates, a ballooning-like character that is not in agreement with ideal-MHD results for the same equilibrium [14]. This may result from the resistivity values imposed in the NIMROD computations, and further study is warranted.

Resolution requirements with the two-fluid electric field and gyroviscosity are more stringent, but the stabilizing effect of diamagnetic rotation leads to a growth-rate spectrum that peaks at moderate n-value. Figure II.8 shows convergence information for our linear two-fluid computations that otherwise have the same parameters of the MHD results in Figs. II.6 and II.7. The most unstable modes have toroidal wavenumbers between 10 and 20. The divergence-error information in Fig. II.8 shows that the n=42 behavior is not converged at these parameters, but computations with *D* increased by a factor of two to 5 m^{2}/s and Δt=2.5×10^{-8} s finds that modes with n≥30 are not growing modes. The resulting growth-rate spectrum for n≤42 is shown in Fig. 9, together with resistive MHD results for the same parameters. Estimating the point of two-fluid stabilization from slab geometry analysis [15] does not explain our threshold. The poloidal

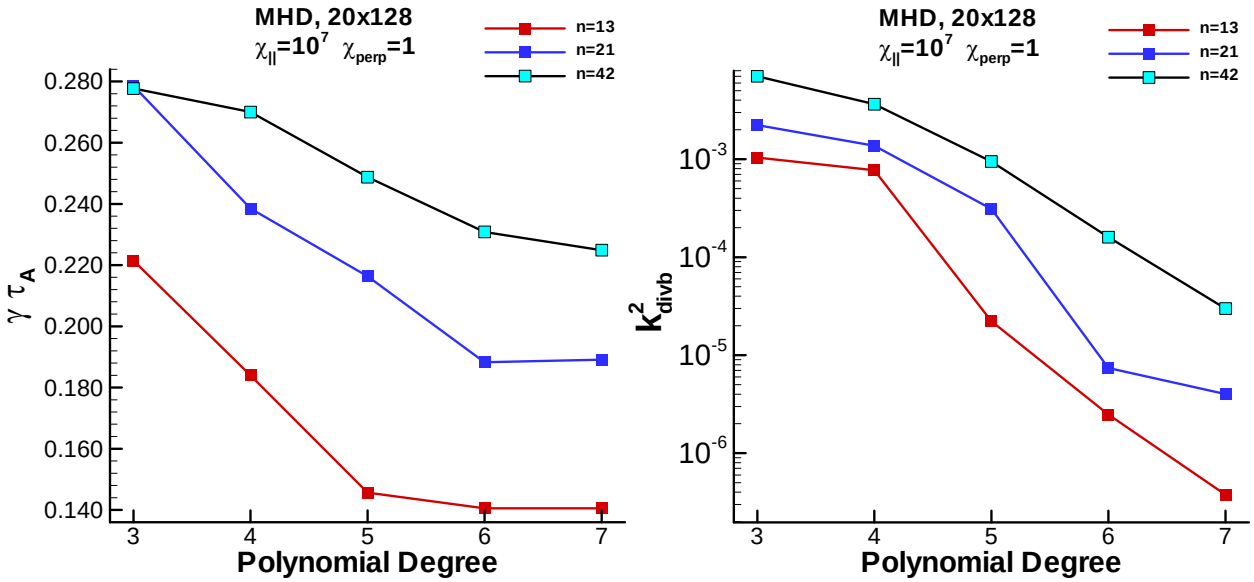

Figure II.6. Computed growth-rate and divergence error for three modes in the MHD spectrum with anisotropic thermal conduction (values should be multiplied by 1.5). The pedestal electrical diffusivity is 7 m^{2}/s, ν=25 m^{2}/s, Δt=5×10^{-8} s, *D*=2.5 m^{2}/s, and κ_{divb}=5×10^{6} m^{2}/s in all cases.

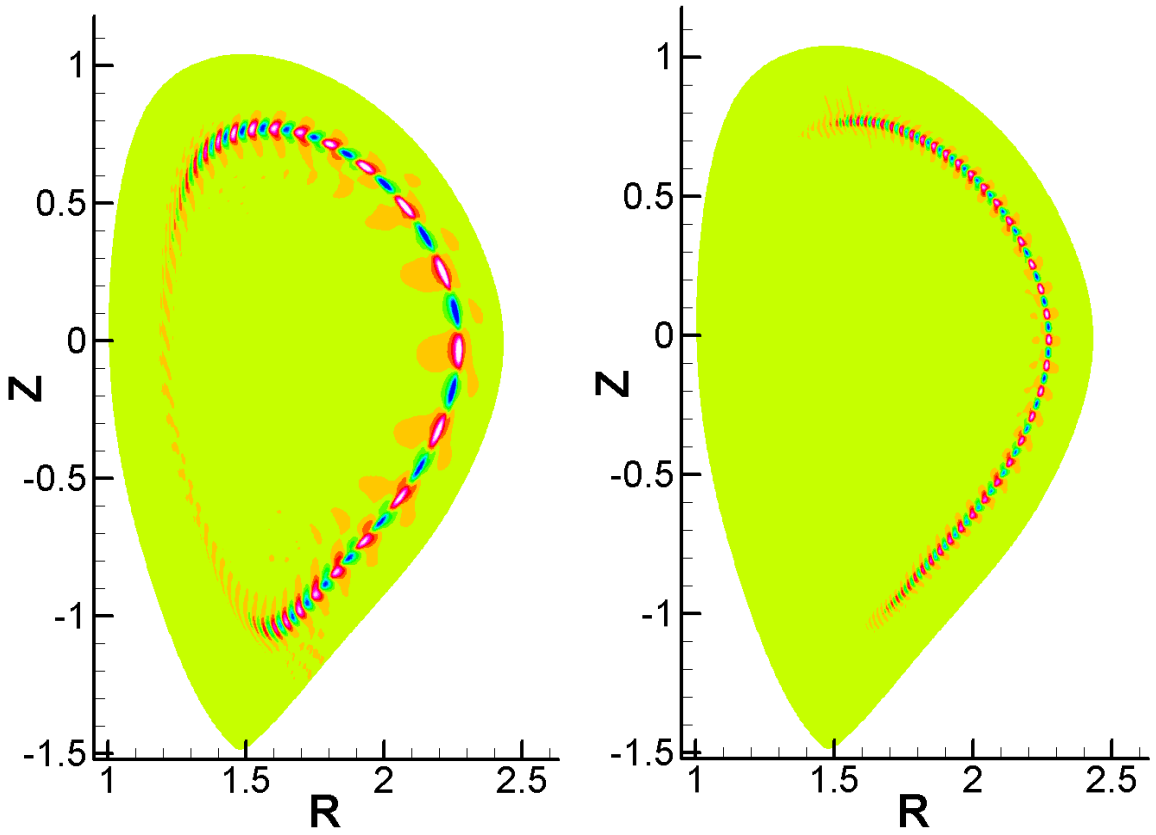

Figure II.7. Toroidal component of flow velocity from the MHD eigenmodes of the n=13 mode (left) and n=42 mode (right), computed with polynomial basis functions of degree 6.

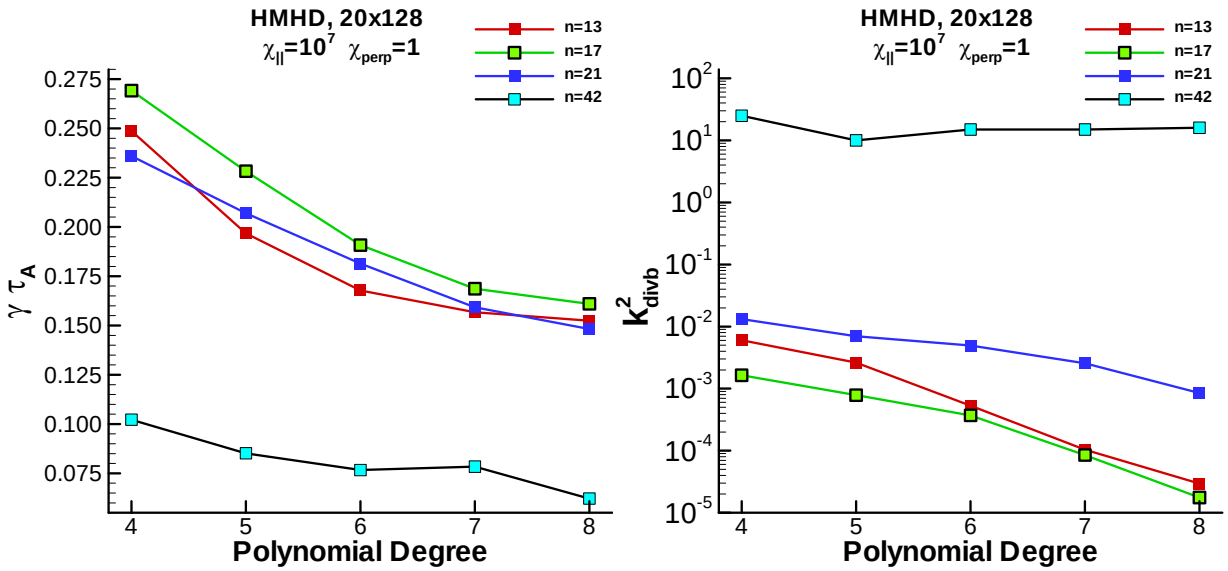

Figure II.8. Growth rate and divergence error for linear two-fluid computations with the same parameters as the MHD cases shown in Fig. 6.

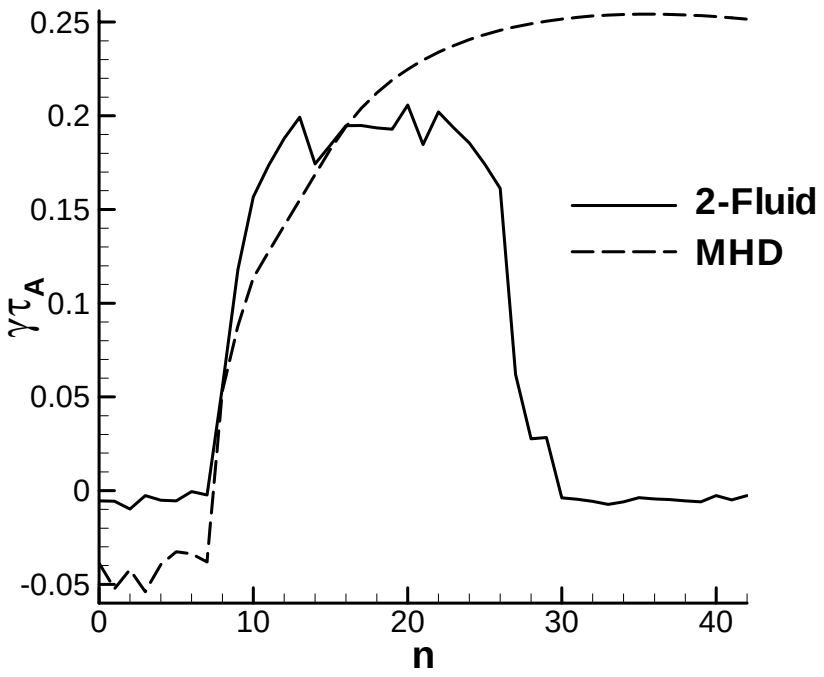

Figure II.9. Comparison of two-fluid and MHD linear growth-rate spectra for toroidal wavenumbers $0 \le n \le 42$ obtained with the 20×120 mesh of biquintic elements (polynomial degree is 5) that is used in the nonlinear two-fluid simulation of Section 5. Numerical parameters include D=5 m^2/s and $\Delta t = 2.5\times10^{-8}$ s.

component of diamagnetic drift velocity ($\mathbf{B}\times\nabla p/neB^2$, plotted in Fig. II.10) peaks at nearly 4×10^4 m/s. With the analytical estimate from Ref. 15 suggesting stability at $\omega_{*i} = mv/r = 2\gamma_{MHD}$, the observed MHD growth-rate of approximately 2×10^5 s^{-1}, minor radius $r \cong 0.5$ m, and q-value of approximately 3, one might expect stability at n=m/q of order unity. However, the radial extent of the diamagnetic drift is narrower than the ELM eigenfunctions, and radial localization is known to reduce the stabilizing effect of ion diamagnetic drift [16]. (In our numerical computation, we have assumed an electrostatic potential profile that makes the ions stationary in the laboratory frame of reference, but ion gyroviscosity is present.) For the modes remaining unstable, two-fluid effects lead to visible distortion of the eigenfunctions. The flow pattern of the n=21 mode, for example, is significantly sheared along the outboard portion of its resonant surface (Fig. II.11), which is the location of peak diamagnetic drift. The growth rate of this mode is 5% smaller in the two-fluid computation than in the MHD computation.

For completeness, temporal convergence information for the two-fluid mode with n=17 is shown in Fig. II.12. The computations have polynomials of degree 6 in a 20×128 mesh and the smaller value of 2.5 m^2/s for the artificial particle diffusivity, D.

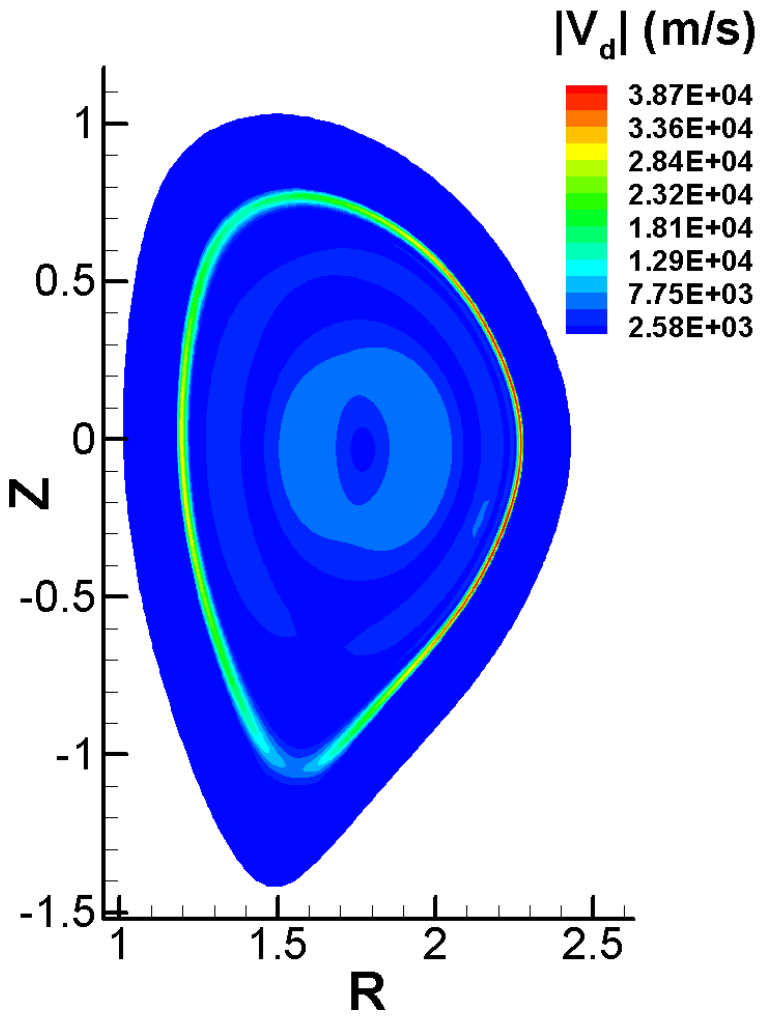

Figure II.10. Magnitude of poloidal diamagnetic drift velocity for DIII-D equilibrium 113317.

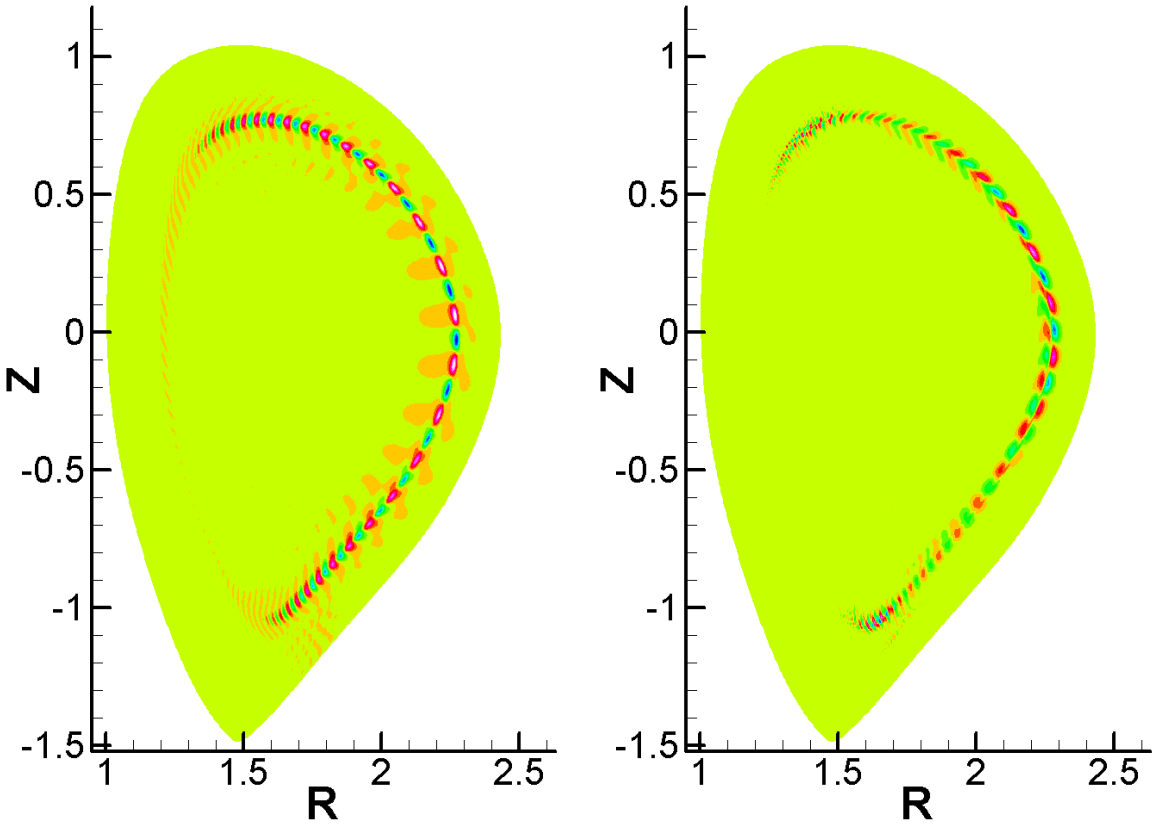

Figure II.11. Two-fluid distortion of the n=21 eigenfunction: the toroidal component of velocity for the n=21 mode is shown for MHD (left) and for the two-fluid model (right). The results shown here are obtained with polynomial basis functions of degree 6.

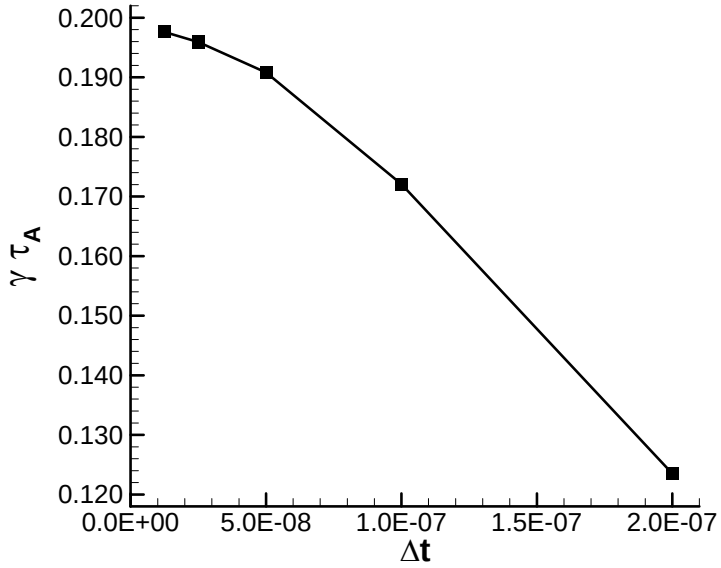

Figure II.12. Temporal convergence of two-fluid linear calculations with n=17, D=2.5 m^2/s, and a 20×128 mesh of elements with basis functions of degree 6.

4. Algorithm Development

Before this fiscal year, the two-fluid implementation had been completed and tested for two-dimensional problems, and an important benchmark of two-fluid interchange stabilization is described in the report for the second quarter of this year.[§] Development completed during this year includes toroidal coupling of nonlinear terms for the Hall electric field, all nonlinear gyroviscosity terms, and an implicit implementation of advection. The algorithm is the "implicit leapfrog" developed for two-fluid modeling in NIMROD [17] with implicit advection terms in the time-advance equation for each field, as required for numerical stability [18]. Our single-temperature temporal algorithm with flow velocity at integer time-indices and all other fields at half-integer time-indices is the following:

$$m_{\mathrm{i}} n^{j+1/2}\left(\frac{\Delta\mathbf{V}}{\Delta t}+\frac{1}{2}\mathbf{V}^{j}\cdot\nabla\Delta\mathbf{V}+\frac{1}{2}\Delta\mathbf{V}\cdot\nabla\mathbf{V}^{j}\right)-\Delta t L^{j+1/2}(\Delta\mathbf{V})+\nabla\cdot\Pi_{\mathrm{i}}(\Delta\mathbf{V}) = \mathbf{J}^{j+1/2}\times\mathbf{B}^{j+1/2}-\nabla p^{j+1/2}-m_{\mathrm{i}} n^{j+1/2}\mathbf{V}^{j}\cdot\nabla\mathbf{V}^{j}-\nabla\cdot\Pi_{\mathrm{i}}\left(\mathbf{V}^{j}\right) \tag{9}$$

$$\frac{\Delta n}{\Delta t}+\frac{1}{2}\nabla\cdot\left(\mathbf{V}^{j+1}\cdot\Delta n-D\nabla\Delta n\right)=-\nabla\cdot\left(\mathbf{V}^{j+1}\cdot n^{j+1/2}-D\nabla n^{j+1/2}\right) \tag{10}$$

$$\frac{3\overline{n}}{2}\left(\frac{\Delta T}{\Delta t}+\frac{1}{2}\mathbf{V}^{j+1}\cdot\nabla\Delta T\right)+\frac{1}{2}\nabla\cdot\mathbf{q}(\Delta T) = -\frac{3\overline{n}}{2}\mathbf{V}^{j+1}\cdot\nabla T^{j+1/2}-\overline{n}T^{j+1/2}\nabla\cdot\mathbf{V}^{j+1}-\nabla\cdot\mathbf{q}\left(T^{j+1/2}\right)+Q^{j+1/2} \tag{11}$$

$$\frac{\Delta\mathbf{B}}{\Delta t}+\frac{1}{2}\mathbf{V}^{j+1}\cdot\nabla\Delta\mathbf{B}+\frac{1}{2}\nabla\times\frac{1}{\overline{n}e}\left(\mathbf{J}^{j+1/2}\times\Delta\mathbf{B}+\Delta\mathbf{J}\times\mathbf{B}^{j+1/2}\right)+\frac{1}{2}\nabla\times\eta\Delta\mathbf{J}-\frac{\kappa_{divb}}{2}\nabla\nabla\cdot\Delta\mathbf{B} = -\nabla\times\left[\frac{1}{\overline{n}e}\left(\mathbf{J}^{j+1/2}\times\mathbf{B}^{j+1/2}-\overline{T}\,\nabla\overline{n}\right)-\mathbf{V}^{j+1}\times\mathbf{B}^{j+1/2}+\eta\mathbf{J}^{j+1/2}\right]+\kappa_{divb}\nabla\nabla\cdot\mathbf{B}^{j+1/2} \tag{12}$$

where L is the semi-implicit operator for MHD dynamics [see Ref. 7], $\mathbf{q}$ is the heat-flux vector, Q represents heating terms (not included in simulations reported here), and the over-bar is the average of the field at the j+1/2 and j+3/2 time-levels. The temporal staggering provides temporal centering for many terms. For the advection term in Eq. (9) and the Hall term in Eq. (12), a Newton-like step provides centering using a linearization from the start of the respective advance at each time-step.

With the spatial representation of high-order finite elements for the poloidal plane and finite Fourier series for the toroidal direction, the implicit equations are advanced with a 'matrix-free' approach. Instead of computing matrix elements associated with implicit terms that couple nonlinear Fourier components, the matrix-vector products needed for Krylov-space solution methods are computed directly. This effectively uses factors of the matrix, applied in a sequence of operations, without finding the product of the matrix factors separately. All such operations for the Hall term, the implicit advection term in each equation, and gyroviscosity have been implemented and tested during FY2006. Matrix elements representing the coupling within the poloidal plane are computed for use in preconditioning the Krylov-space solves, and a significant

[§] Available from http://w3.pppl.gov/cemm/Milestones/ELM_Milestone2006Q2_01.pdf .

amount of the associated development was also completed during FY2006. (Preconditioning is discussed further in Sect. 6.) At this point, the NIMROD code has a fully functional, implicit three-dimensional two-fluid advance for low-frequency dynamics. Relatively minor development is still needed for advancing separate ion and electron temperatures in nonlinear simulations.

The local distortion of large pedestal gradients that occurs during ELMs is a somewhat unique condition for magnetic-confinement. To address this in the computations, nonlinear numerical diffusion operators, such as

$$-f\,\nabla\cdot\left[\left(\frac{\Delta t\,\mathbf{V}\cdot\nabla n}{n}\right)^2\left(\frac{A_e}{\Delta t}\right)\frac{\mathbf{VV}}{V^2}\cdot\nabla n\right],$$

have been added to the number density and temperature advances; A_e is the element area, and f is a parameter of order 0.01-0.1. The time-centered implicit advection does not introduce numerical dissipation otherwise, but its numerical dispersion can lead to well-known overshoot oscillations when advecting large gradients. The above nonlinear numerical diffusion arises only where dispersion error is large, like explicit upwinding methods, and this approach is applied in the two-fluid simulation described in Sect. 5. [Test information is available in the report for the third quarter of this fiscal year.[**]]

5. Nonlinear Results

Over FY2006, the NIMROD team has performed nonlinear simulations of ELM events using the MHD model with and without flow and using the two-fluid model, i.e. with Hall and electron pressure-gradient terms in the electric field and Braginskii gyroviscosity in the ion stress. Toroidal resolution of 40 modes, as required for the milestone, has been applied in MHD simulations without flow and in the two-fluid simulation. All of the simulations use the number density profile from the equilibrium information in the equilibrium file for the DIII-D discharges. In the 40-mode two-fluid simulation, the evolving three-dimensional number density distribution is used for computing inertia in the velocity advance and for heat capacity and thermal conductivity in the temperature advance. The MHD simulations use an approximation of these terms that is based on the equilibrium density profile. Similarly, the resistivity in the two-fluid simulation is computed from the local three-dimensional evolving temperature, whereas the MHD computations use the toroidal average of the evolving temperature distribution. The nonlinear MHD computations were performed before the implementation of the nonlinear numerical diffusivity for advection. Without it, overshoot oscillations easily produce unphysical negative number densities when using the experimental profile. To avoid this condition, a large value of 2500 m^2/s is used for the global artificial particle diffusivity D. In contrast to the conclusions reached in Ref. 19, we find that this diffusivity stabilizes interchange modes at large toroidal wavenumbers, producing a spectrum that approximates the two-fluid spectrum. The global diffusivity is set to 5 m^2/s in the two-fluid simulation to avoid noise at the node-spacing scale.

The nonlinear MHD computations have been reported in the second and third quarterly reports for this year and are summarized here for completeness. They have a domain that is extended beyond the location of the experimental wall to allow analysis of heat and mass flux at that location without interference from no-slip conditions applied to the flow velocity at the wall.

[**] Available from http://w3.pppl.gov/cemm/Milestones/Q3_elm_mile06.pdf .

Such computations have been performed for DIII-D discharges 113207 and 113317. With the large value of *D*, the linear spectrum peaks at n=14 for the 113207 equilibrium and at n=12 for the 113317 equilibrium. In the early nonlinear phase of the simulations, two-wave coupling of unstable modes generates perturbations at wavenumbers near unity and at wavenumbers that have n in the vicinity of twice that of the peak of the spectrum. This is evident in Fig. 13, along with three-wave coupling at the largest wavenumbers from the peak of the spectrum beating with its first harmonic. This exponential growth changes when nonlinear perturbations approach the magnitude of the background. Figure 14 shows this transition in the evolution of the magnetic fluctuation spectrum. Ribbons of hot plasma emerge from the confined plasma during this transition and later extend to the location of the physical wall (Fig.II.15).

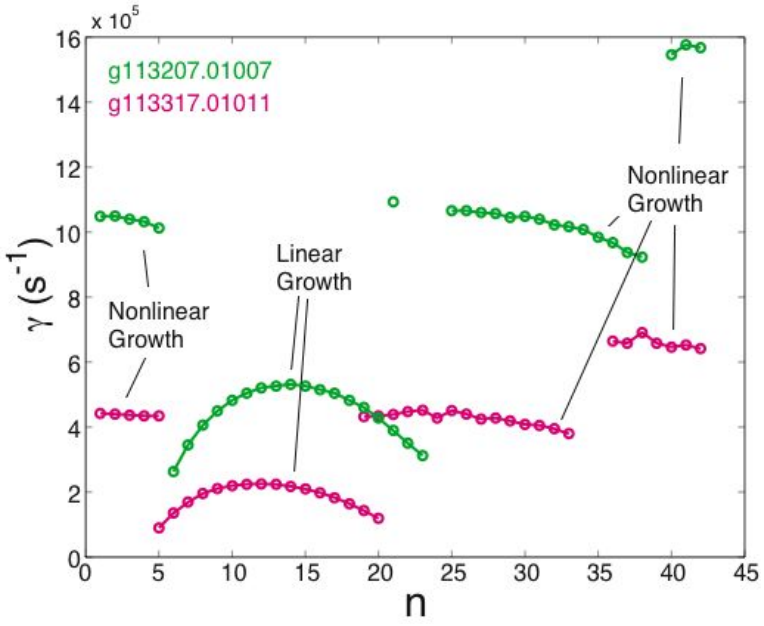

Figure II.13. Growth rates measured from the early nonlinear phase of the MHD simulations for the two equilibria. Here, the growth rate for each wavenumber is not an eigenvalue but the diagnostic: $0.5 \times d\ \ln(\text{fluctuation energy})/dt$.

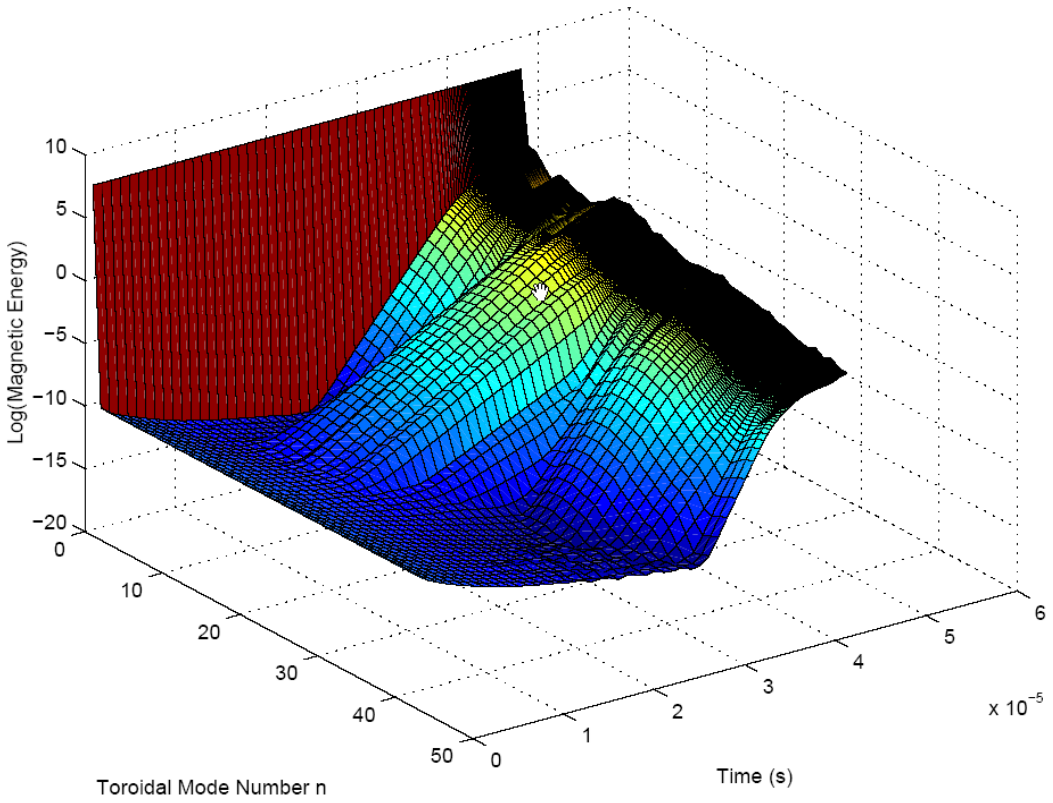

Figure II.14. Evolution of magnetic fluctuation energy in the nonlinear MHD simulation for discharge 113207.

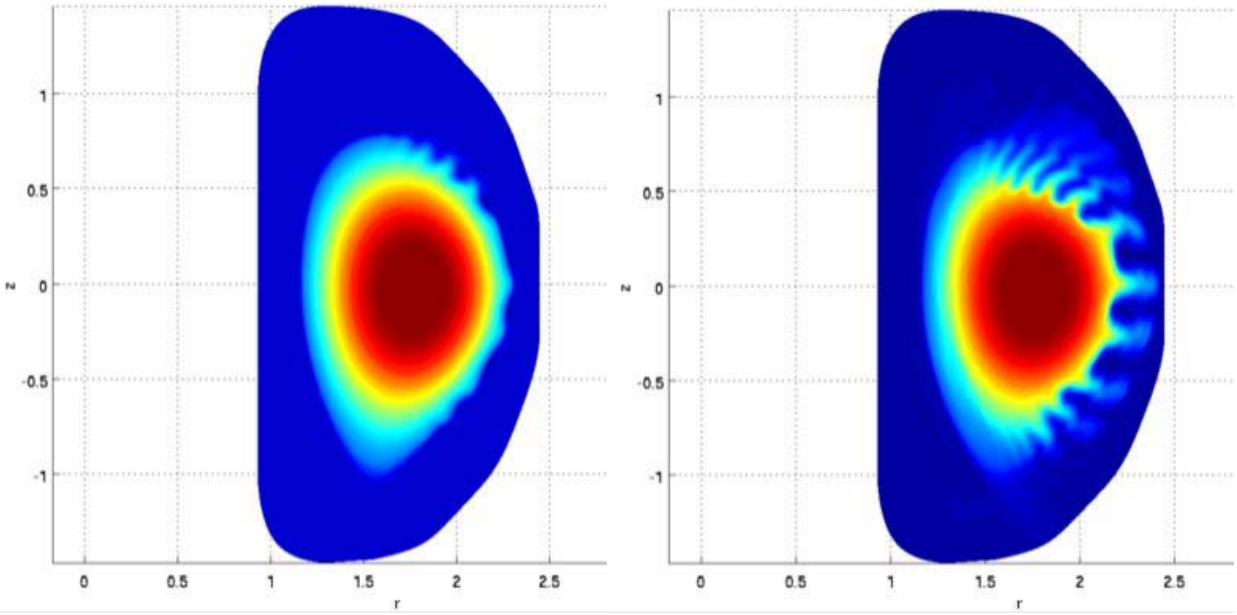

Figure II.15. Color contours of constant temperature at fixed toroidal location from the MHD computation for the 113207 equilibrium during the transition phase (left) and in the late nonlinear phase (right). Each protrusion of hot fluid and incursion of cold fluid in the cross-section plot extends as a helical band on the outboard side of the torus.

The existence of the edge transport barrier, hence the large gradients inside the separatrix, is attributed to large-scale toroidal plasma flow inside the separatrix. The gradient of this flow itself can affect the ELM perturbations, and we have investigated this through linear and nonlinear MHD computations with wavenumbers $0 \le n \le 21$. Using a model flow profile with experimentally relevant magnitude of order 10^5 m/s (Fig. II.16a), we find an increase of linear growth rates of approximately 20%, possibly due to a Kelvin-Helmholtz effect. However, as shown in Fig. II.16b, the flow is effective at shearing the ribbons of high temperature in the late nonlinear phase.

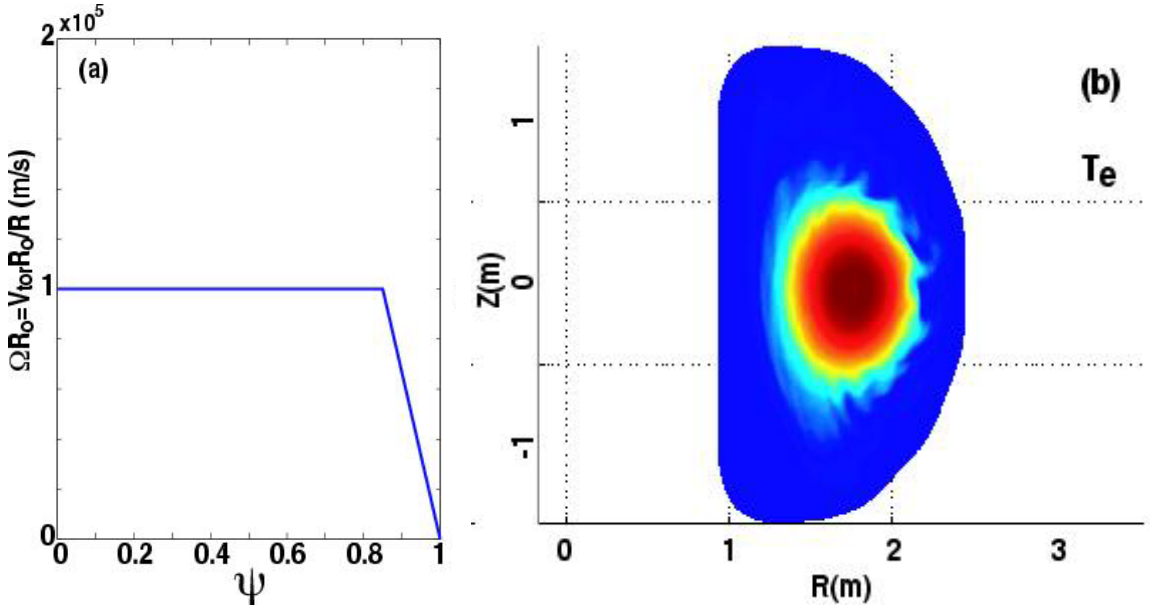

Figure II.16. Model flow profile within the separatrix (a) and color contours of constant temperature at fixed toroidal angle in the late nonlinear phase (b) for the MHD computation with flow.

The two-fluid computation is based on the equilibrium data for DIII-D discharge 113317, has dissipation coefficients of $\chi_{\parallel}=1.5\times10^7$ m^2/s, $\chi_{\perp}=1.5$ m^2/s, and $\nu=25$ m^2/s, and uses a poloidal mesh of 20×120 biquintic finite elements. At this resolution and $D=2.5$ m^2/s, linear growth rates are accurate to 35% in comparison to the converged results in Fig. II.8. ($D=5$ m^2/s in the nonlinear computation.) Our present implementation of the SuperLU solver library [20] leads to memory limitations on the IBM SP5 machine 'Bassi' at the Nation Energy Research Scientific Computing Center (NERSC) when running NIMROD with basis functions of degree greater than five on this mesh. The quantitative error from the reduced resolution does not affect the shape of the linear spectrum, however, and we expect the primary features of the nonlinear evolution to be valid at least qualitatively. Initial conditions use the results of the linear two-fluid spectrum computation shown in Fig. II.9. The perturbation energies are slightly peaked toward the low end of the unstable group of modes, because they are first to emerge from the random perturbations used to initiate the linear calculations and thus have a head start in the nonlinear computation. Their amplitude at the beginning of the nonlinear computation is a somewhat

arbitrary choice, as long as it does not lead to strong nonlinear effects immediately. The evolution of kinetic fluctuation energies over the first nonlinear time-steps shows two-wave coupling producing a high-n harmonic of the spectrum peak and coupling to n-values below 10 (Fig. II.7), but significant growth still follows before distortions of the pedestal gradients become apparent.

In the final state of the two-fluid computation achieved for the milestone, the fluctuations are growing at a decreasing rate, and density and temperature perturbations approach the pedestal values for number density and temperature. From configuration space, we observe that the perturbations do not extend over the entire outboard side of the torus, unlike our MHD results. Instead, they are grouped into a helical band, as shown in Figs. II.18 and II.19. Like conditions in the reversed-field pinch (RFP), the largest modes are neighbors in the n-spectrum, and their two-wave interactions generate n=1 perturbations [21]. Unlike the RFP, the different modes are resonant at essentially the same *q*-value, so the nonlinear structure is of single helicity with respect to winding around the torus. In the 113317 equilibrium, the ELMs are resonant near q=3, and the poloidal cross-section (Fig. II.18) shows three groups of perturbations: one near the separatrix, another on the outboard side above the midplane, and the third at the top of the separatrix. With respect to nonlinear coupling to low-n leading to localization, this result shares features found with the reduced-Braginskii model applied to harmonics of n=5 [4]. Although it is not filamentary, the nonlinear structure in our full-geometry computation covers only a small fraction of the toroidal angle. We note, however, that while the phases of the initial perturbations have not been prearranged, it remains to be verified that such localization is the result of phase locking during the evolution.

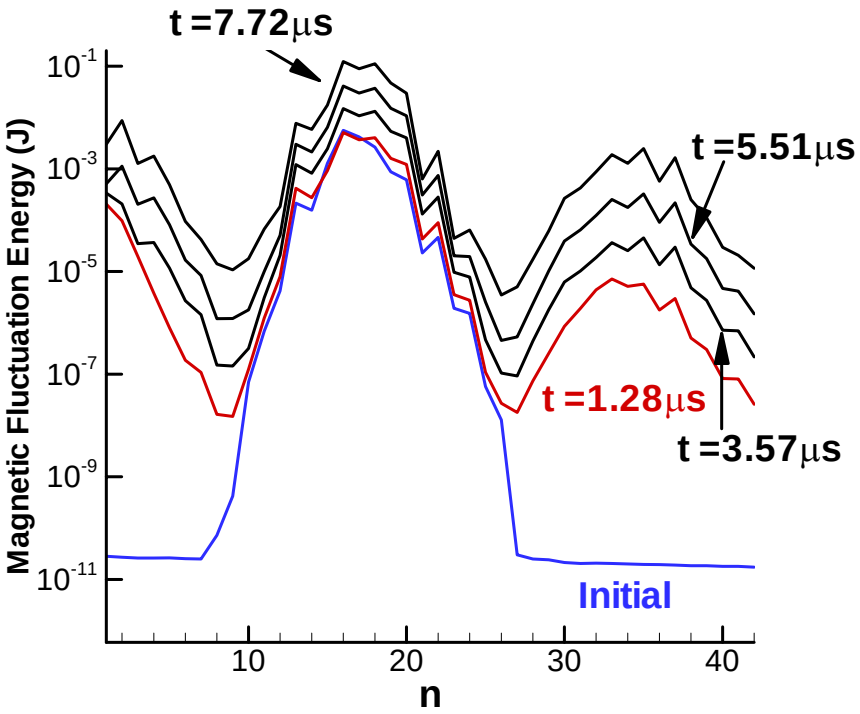

Figure II.17. Evolution of the magnetic fluctuation energy from the two-fluid computation. The initial state is from the linear two-fluid spectrum calculation, and times are with respect to the start of the nonlinear simulation.

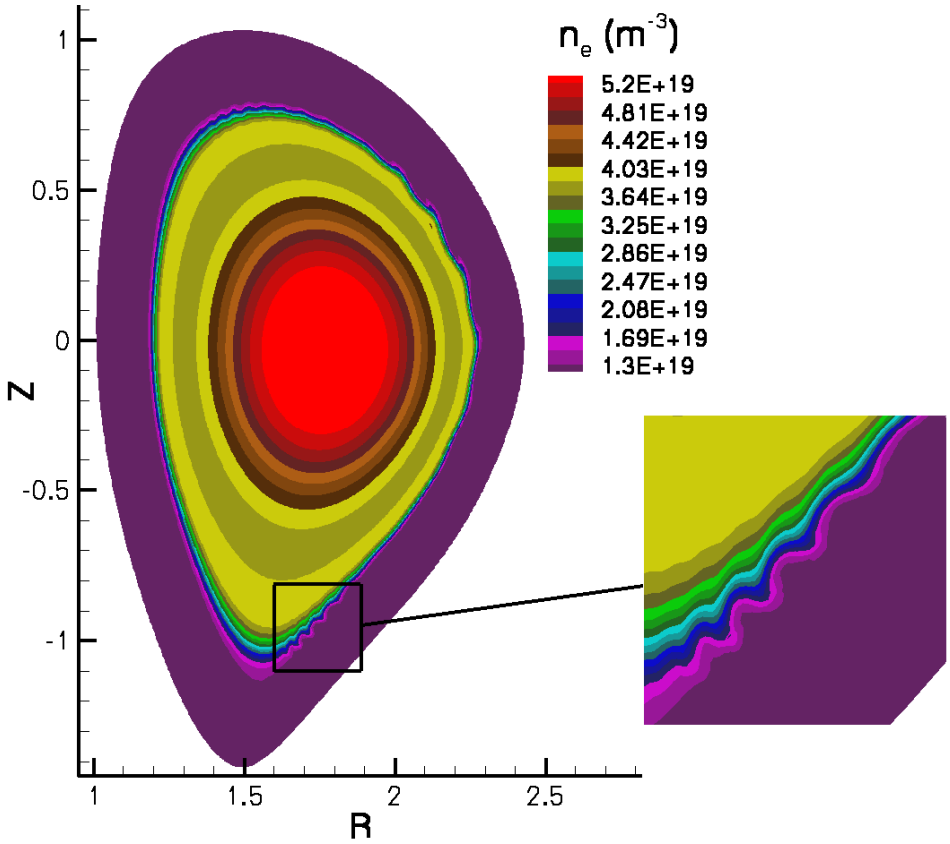

Figure II.18. Number density at toroidal angle ϕ=0 at 7.92 μs into the nonlinear two-fluid computation.

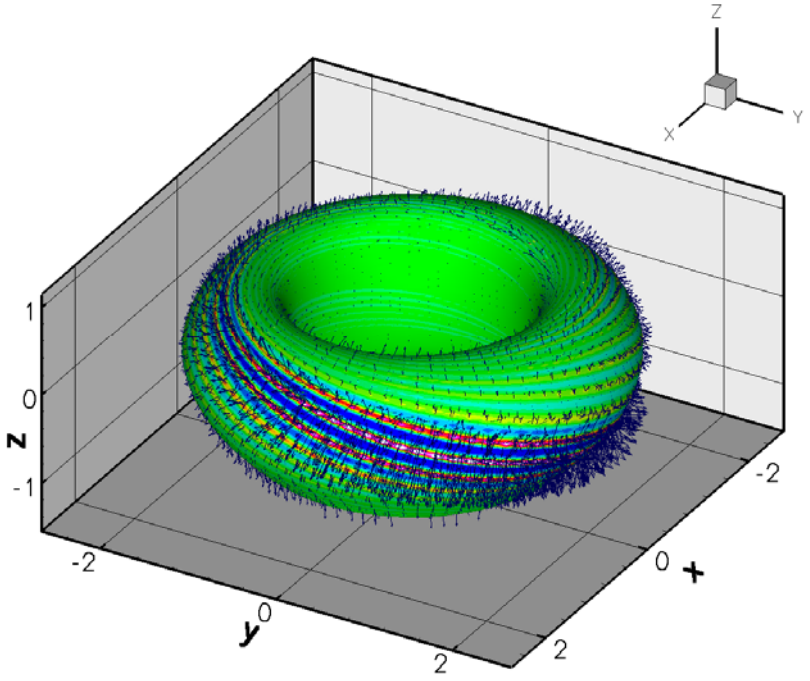

Figure II.19. Temperature perturbations along the surface where n=3×10^{19} m^{-3} at 7.72 μs into the nonlinear two-fluid computation. The maximum temperature perturbation is 100 eV, 25% of the pedestal temperature. Perturbed flow velocity vectors are superposed.

6. Discussion and Conclusions

The results reported here represent significant numerical progress in the modeling of nonlinear ELM evolution. The physical insights on the impact of two-fluid effects and large-scale flows are likely to be just among the first from a continuing computational physics investigation. However, this milestone effort has had equal value as an exercise in what will be required to move NIMROD to the peta-scale computing level. The spatial representation used for the large nonlinear two-fluid computation has the equivalent of more than 5.1 million space points—estimated from 2400 elements with 25 basis nodes each (neglecting extra surface nodes) multiplied by 43 Fourier components and a factor of two for real and imaginary parts. As vector equations, the velocity and magnetic-field advances solve linear systems for more than 7.5 million coupled complex quantities at each time-step. The computation required fifteen 12-hour segments on the IBM SP5 at NERSC using 344 processors (nearly 40% of the machine) that are rated at 7.6 GFlops/s each. NIMROD's internal timer reports that approximately 75% of the CPU time is spent iterating solutions of the large sparse algebraic systems. Moreover, in all but the first segment of the nonlinear simulation, the time-step had to be limited well below accuracy requirements to ensure that these iterations converge. (Decreasing the time-step reduces matrix condition numbers.) Toward the end of the computation, the time-step is restricted to 1/20 of the value needed for accurate growth rates, according to Fig. II.12. If this had not been the case, we would have been able to run the simulation much farther into the nonlinear phase.

Two physical aspects of the two-fluid ELM problem distinguish it from the many previous applications of the NIMROD code. First, the mathematical operators that are used to advance implicitly the Hall effect, the gyroviscous stress, and advection are not self-adjoint. Through the spatial representation, these operators become large non-Hermitian matrices that require an appropriate iterative method. We use a Generalized Minimum Residual algorithm (GMRES, Ref. 22), which is considered the most effective iterative method for many non-symmetric and non-Hermitian linear systems. A fundamental aspect of the algorithm is that it stores a vector at each iteration cycle and explicitly orthogonalizes the next vector with respect to all previous. In our case, each vector has more than 7.5 million complex components. The second new aspect of the ELM problem is the large range of unstable wavenumbers, which leads to strong coupling among many toroidal modes. While nonlinear coupling among toroidal modes is important in other NIMROD applications, it has not been as dominant as the coupling associated with the nonlinear Hall terms (representing nonlinear whistler waves) in the magnetic advance. Thus, toroidal coupling in the operators used for preconditioning the iterations has not been needed. It will be essential for continuing the nonlinear two-fluid ELM study. Even with the limited time-step, the present scheme uses approximately 200 iterations to solve the system for the magnetic-field advance when keeping and orthogonalizing 120 iteration vectors. This is quite costly for our system size, but the GMRES iteration does not converge when retaining fewer vectors (50) in this computation.

While the nonlinear two-fluid simulation is large by present-day implicit MHD standards, we note that the resolution is still rather marginal, even with the resistivity profile multiplied by a factor of 100 over the Spitzer calculation. The linear computations show that accuracy can be improved with basis functions of larger polynomial degree, and the toroidal representation with $0 \le n \le 42$ only captures the first group of harmonics in the nonlinear simulation. Moreover, the mesh (shown in Fig. II.3) is tailored for dynamics just near the location of the separatrix. There are not enough elements in the edge region to resolve a late nonlinear phase if dynamics extend

to the wall, as in the MHD simulations. Any coupling to dynamics in the core would also need more resolution. These considerations motivate computation at a yet much larger scale, but they also demand further refinement of our algorithm. The development priorities that have arisen from this milestone exercise are:

1) *Toroidal coupling in the preconditioning operation*—this has been noted above.
2) *Adapting the less memory intensive interface to the SuperLU library*—most of this has been completed as part of the milestone development.
3) *Conversion to parallel i/o*—data files are presently written through the master node, which requires large amounts of message passing. This did not impede the milestone computation, but it now appears to be an impending bottleneck for larger computations if not addressed.
4) *Improved spatial representation for interchange behavior*—methods developed for spectral element computations of incompressible flow may be able to avoid noise without global particle diffusivity.

The NIMROD Team looks forward to working on these critical issues for peta-scale computing as part of the effort for integrated modeling of burning plasmas.

III. Computational Studies with the M3D code

In this quarter we carried out large scale *40* toroidal mode simulations. The simulations were done using the shared memory *256* processor ram.ccs.ornl.gov and the distributed memory *6000+* processor seaborg.nersc.gov. The shared memory version of M3D reads an EFIT eqdsk file and produces a mesh. The particular case chosen was the DIII-D equilibrium reconstruction *g113207*. The mesh and equilibrium data are written out in a suitable file format which is used to initialize the MPP version.

An upwind advection algorithm was introduced in M3D to prevent negative density, which can occur when there is strong advection of the density pedestal. The following simulations benefited from the use of upwinding.

Simulations were done in an outer annulus of plasma, from normalized radius $\rho = 0.8$ to the wall, where

$$\rho = \left[\left(\psi - \psi_{axis} \right) \Big/ \left(\psi_{separatrix} - \psi_{axis} \right) \right]^{1/2}.$$

In the initial eqdsk file, the density is only given out to the separatrix. The density was extended out to the wall by assuming that the density in the open flux surface region is constant and equal to its value at the separatrix.

The initial state was perturbed and a single *n = 12* mode was obtained. The growth rate was $\gamma = 0.24\tau_A^{-1}$, where $\tau_A = R/V_A$, R is the major radius, and V_A is the Alfvén speed.
This was used to initialize nonlinear runs with toroidal mode numbers *n = 0, ... 40.* No modes were omitted; the full torus was included. In the *(R,Z)* plane, a mesh of *18,000* points was used. A close-up of the *(R,Z)* mesh, which is connected with triangular
finite elements, is shown in Figure III.1.

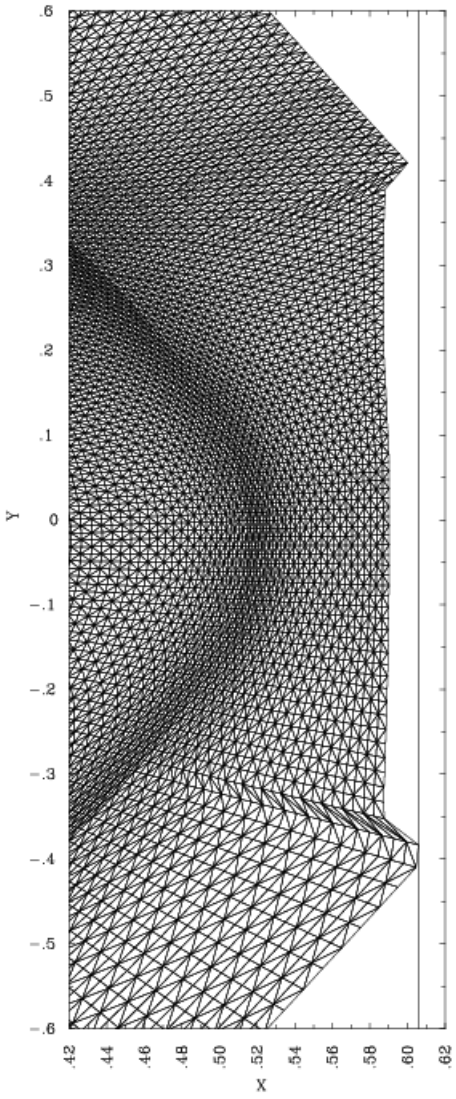

Figure III.1: A part of the (R,Z) mesh.

In the linear and nonlinear runs, $S = \tau_{resistive} / \tau_A = 10^6$, and the Prandtl number was 10.

The initial equilibrium poloidal flux ψ is shown in Figure III.2(a), and the linear perturbed ψ in Figure III.2(b).

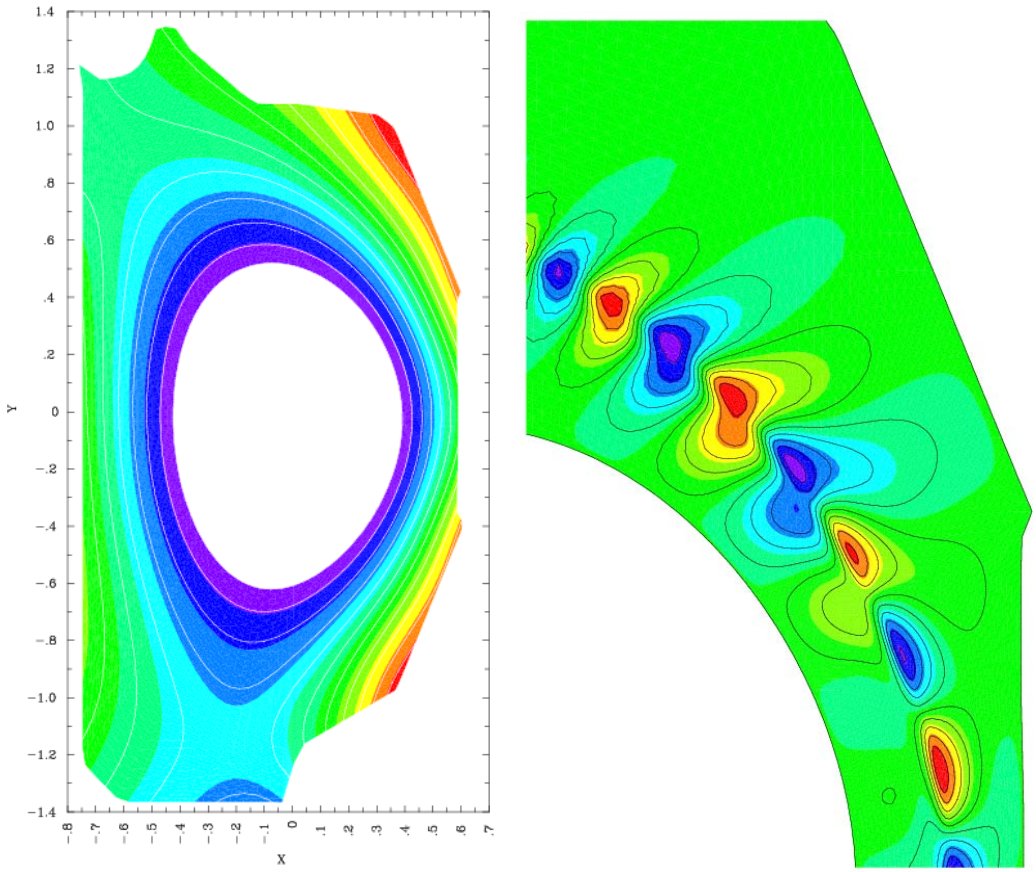

Figure III.2 (a) Equilibrium poloidal magnetic flux ψ of g113207. (b) Close-up of contours of linear ψ perturbations with toroidal mode number *n =12.*

To compare with MKS units, the reciprocal Alfvén time is

$$\tau_A^{-1} = \frac{V_A}{R} = \frac{F_{pol}}{R^2(\mu n M_i)^{1/2}}.$$

Here $F_{pol} = 3.7m - T$, $R = 1.76m$, $\mu = 4\pi 10^{-7}\, Hm^{-1}$, and the mass density on axis is 3.4×10^{-7} Kg $m^{-3.}$. This gives $\tau_A^{-1} = 1.8 \times 10^6\, s^{-1}$.

In the nonlinear runs, gyroviscosity, a two fluid effect, was included. The strength of two fluid effects is measured by the Hall parameter

$$H = \frac{c}{\omega_{pi} R},$$

the ratio of the ion skin depth to the major radius. The value *H = 0.02* was assumed, consistent with DIII-D experiments. This value of *H* was found in previous linear simulation to be able to stabilize modes with toroidal mode number of order *n = 30*.

Nonlinear pressure contours are shown in Fig. III.3. The pressure is shown at times $t = 6.7\tau_A$, $t = 23.4\tau_A$, and $t = 30.2\tau_A$.

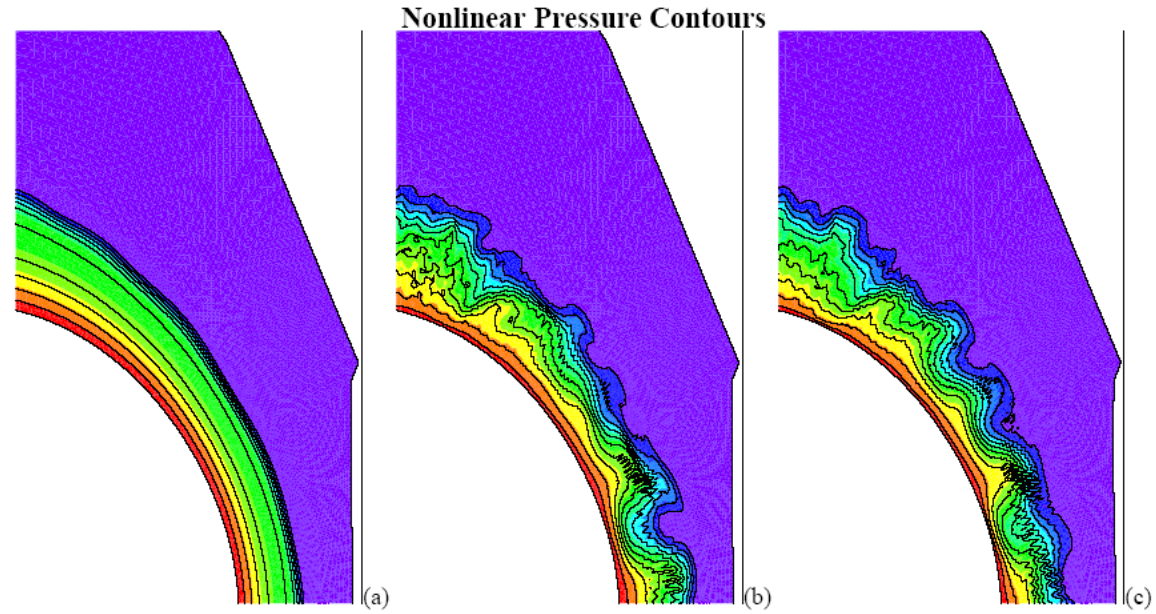

Figure III.3 Close-up of pressure contours in the plane $\phi = 0$ at (a) $t = 6.7\ \tau_A$, (b) $t = 24.3\ \tau_A$, and (c) $t = 30.2\ \tau_A$

Nonlinear density contours are shown in III.4, at the same times as the previous figures.

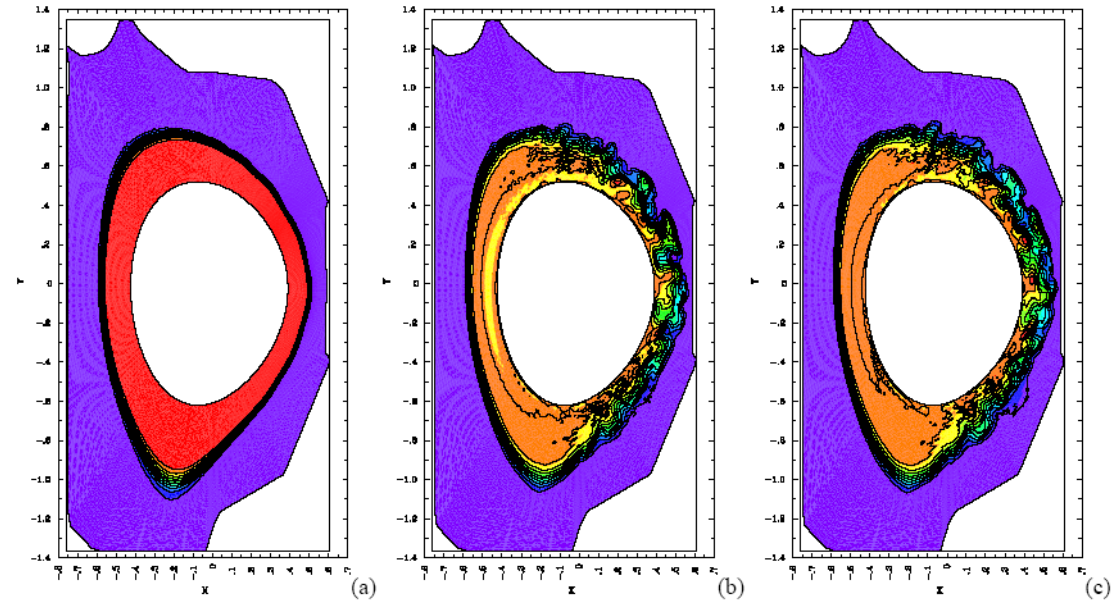

Figure III.4 (a) density contours in the plane $\phi = 0$ at (a) $t = 6.7\ \tau_A$, (b) $t = 24.3\ \tau_A$, and (c) $t = 30.2\ \tau_A$

The nonlinear density profiles that correspond to Figure III.4. are shown in Figure III.5..
These are slices from the contour plots through the midplane at *Z=ϕ=0,*along the major radius *R*.
It is remarkable that there is such a large density ejected all the way out to the wall.
Density perturbations extend across the initial separatrix at *R=0.52* and persist in the open field line region. The density gradient relaxes to a lower value inside the separatrix.

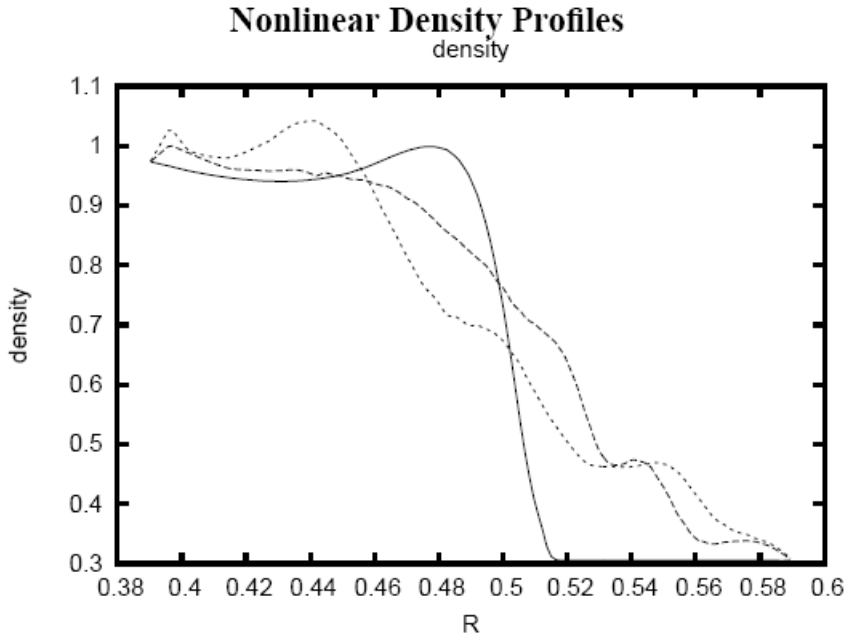

Figure III.5: Density perturbations extend across the initial separatrix at *R=0.52* and persist in the open field line region. The density gradient relaxes to a lower value inside the separatrix. Solid line: $t = 6.7\ \tau_A$**, dashed line:** $t = 24.3\ \tau_A$**, dotted line:** $t = 30.2\ \tau_A$**.**

The temperature perturbations are much less than the density perturbations. Evidently this is consistent with experimental observations of ELMs, that the temperature profile is hardly affected by the ELM, while the density is strongly affected. In Figure III.6 are shown the temperature profiles as the same times as before.

The main reason for the difference between density and temperature evolution is the large parallel thermal conductivity, which rapidly equilibrates the temperature on open magnetic field lines to the wall temperature. Evidently plasma is able to cross from closed magnetic field lines inside the magnetic separatrix to open field lines outside the magnetic separatrix. When three dimensional magnetic perturbations are present, the magnetic separatrix becomes ill defined, stochastically connecting regions of closed and open magnetic field lines. Plasma in the original separatrix region is poorly confined.

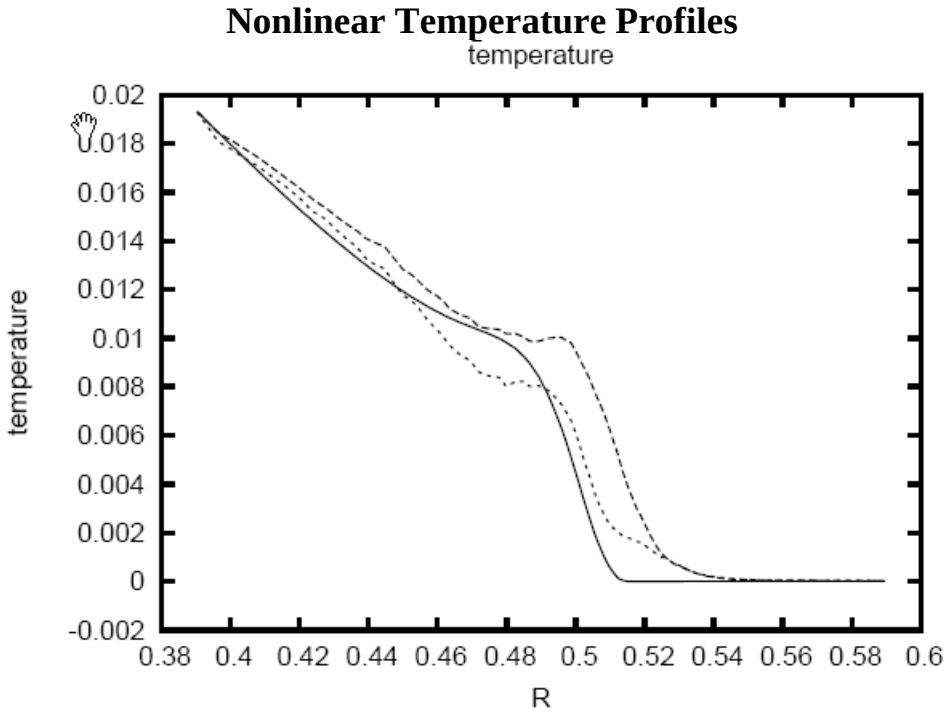

Figure III.6. Temperature profiles at the same times as in the contour plots. Note that the temperature profile changes only slightly, compared with the density. Solid line: $t = 6.7\,\tau_A$**, dashed line:** $t = 24.3\,\tau_A$**, dotted line:** $t = 30.2\,\tau_A$**.**

The pressure profile perturbations are intermediate between density and temperature perturbations as seen in Figure III.7.

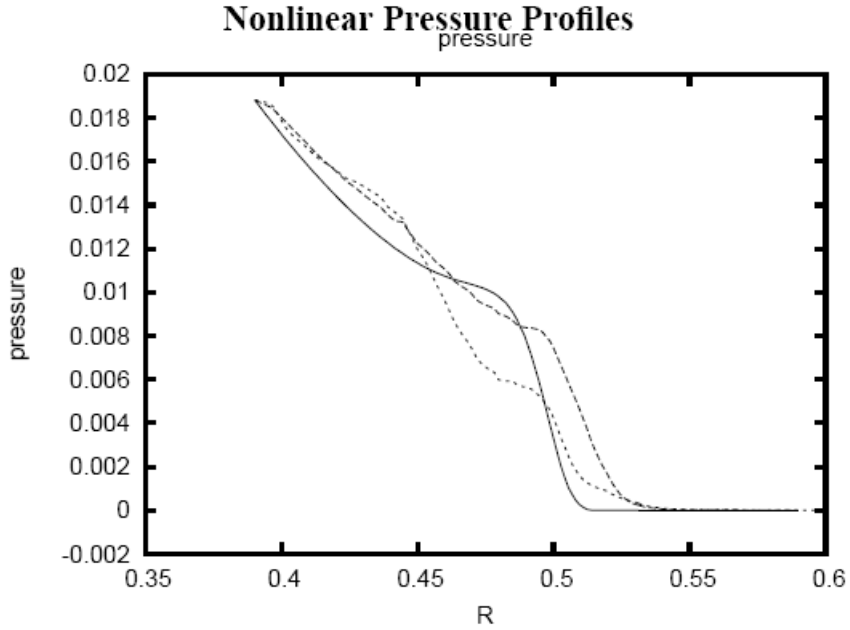

Figure III.7. Pressure profiles at the same times as in the contour plots. Solid line: $t = 6.7\,\tau_A$**, dashed line:** $t = 24.3\,\tau_A$**, dotted line:** $t = 30.2\,\tau_A$**.**

The toroidal current density profile initially has a relatively narrow bootstrap current profile. This broadens and decreases in amplitude with time. This is consistent with the decrease of the pressure gradient.

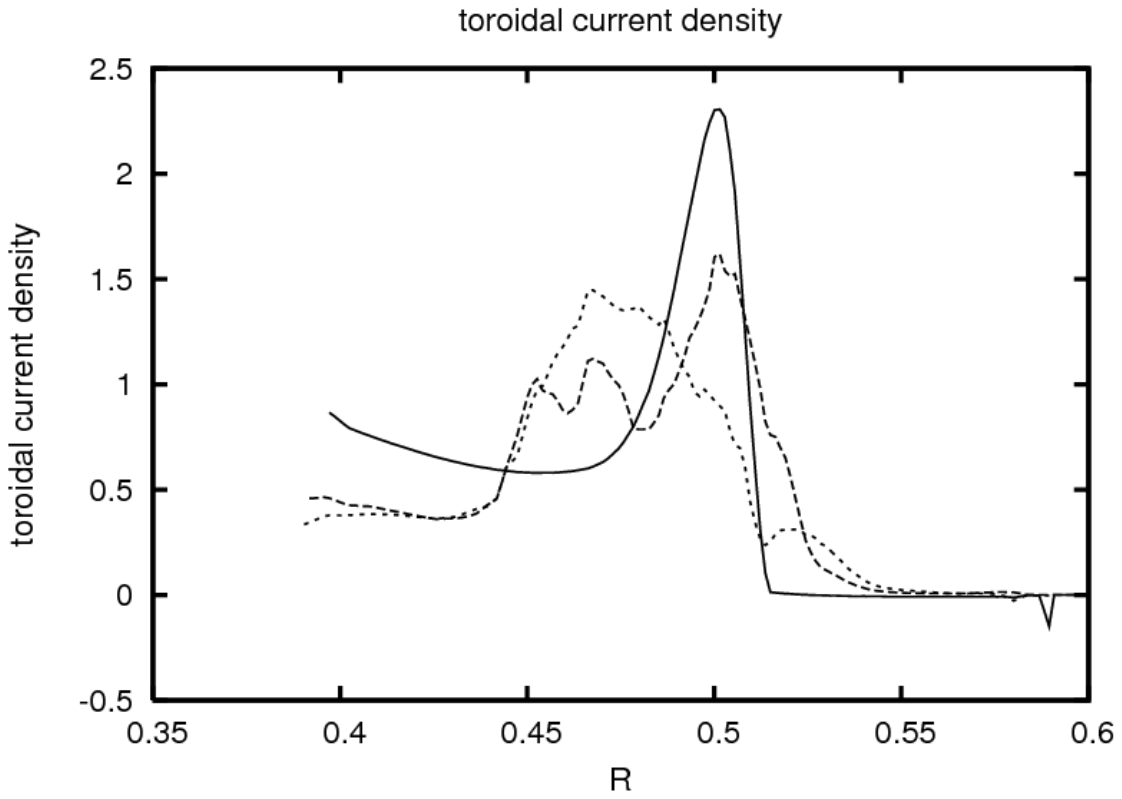

Figure III.7. Toroidal current density profiles at the same times as in the contour plots. Solid line: $t = 6.7\,\tau_A$**, dashed line:** $t = 24.3\,\tau_A$**, dotted line:** $t = 30.2\,\tau_A$

IV. Summary

This report describes high resolution studies of ELM events in tokamaks using two of the most comprehensive Extended MHD codes available, NIMROD and M3D. The incorporation of the two-fluid model and the high resolution requirements for ELM modeling presented new computational challenges in the area of solver efficiency and developing special algorithms to maintain positive densities.

It has now been verified by both NIMROD and M3D that the two-fluid effects, primarily the gyroviscosity, provides a cutoff that selectively stabilizes short wavelength modes. It is also evident that the nonlinear evolution of these modes is quite rich and more work needs to be done before definitive conclusions can be reached. Nevertheless, several interesting observations resulted from this work.

The NIMROD two-fluid calculations find that the nonlinear perturbations tend to group into a helical band, although the dependence of this result on the details of the initial conditions need to be further explored. The M3D two-fluid calculations find that density perturbations are significantly larger than the temperature perturbations for the same calculation, and that a substantial fraction of the edge plasma is able to cross from closed magnetic field lines inside the magnetic separatrix to open field lines outside the magnetic separatrix.

It is significant that these preliminary high-resolution results have been obtained. However a complete understanding of the details of the many different types of ELM behavior will only come after many similar studies are performed, presumably with even more powerful computers and algorithms than are now available.

Acknowledgments

The authors wish to thank Chris Hegna and Jim Callen of the University of Wisconsin and Phillip Snyder of General Atomics for many helpful discussions on physics relevant to ELMs. The authors also wish to thank Tom Osborne of General Atomics for assistance with the equilibrium information, Xiaoye Li of Lawrence Berkeley Laboratory for assistance with the SuperLU parallel software library, and David Keyes, Mark Adams, and other members of the TOPS SciDAC group for expert assistance in the optimization of the solver routines in M3D..

This work was supported by DOE grant numbers DE-FC02-02ER54668, DE-FC02-04ER54798, DE-FC03-02ER54666, DE-FG03-95ER54309, DE-FG02-04ER54799, DE-FC02-04ER-54801, DE-FG02-04ER54802, and DE-AC02-76CH03073. This research used resources of the National Energy Research Scientific Computing Center (NERSC), which is supported by the Office of Science of the U.S. Department of Energy under Contract No. DE-AC02-05CH11231 and of the National Center for Computational Sciences (NCCS) at the Oak Ridge National Laboratory.

References

[1] P. B. Snyder, H. R. Wilson, J. R. Ferron, L. L. Lao, A. W. Leonard, T. H. Osborne, A. D. Turnbull, D. Mossessian, M. Murakami, and X. Q. Xu, "Edge localized modes and the pedestal: A model based on coupled peeling--ballooning modes," Physics of Plasmas **9**, 2037 (2002).

[2] H. R. Wilson, P. B. Snyder, G. T. A. Huysmans, and R. L. Miller, "Numerical studies of edge localized instabilities in tokamaks," Physics of Plasmas **9**, 1277 (2002).

[3] H. R. Strauss, "Edge-localized mode simulations in divertor tokamaks," Physics of Plasmas **3**, 4095 (1996).

[4] P. B. Snyder, H. R. Wilson, and X. Q. Xu, "Progress in the peeling-ballooning model of edge localized modes: Numerical studies of nonlinear dynamics," Physics of Plasmas **12**, 056115 (2005).

[5] L. L. Lao, J. R. Ferron, R. J. Groebner, W. W. Howl, H. E. St John, E. J. Strait, and T. S. Taylor, Nuclear Fusion **30**, 1035 (1990).

[6] J. L. Luxon, *et al.*, Plasma Physics and Controlled Nuclear Fusion Research 1986, Vol. 1, 159 (IAEA, Vienna, 1987).

[7] C. R. Sovinec, A. H. Glasser, D. C. Barnes, T. A. Gianakon, R. A. Nebel, S. E. Kruger, D. D. Schnack, S. J. Plimpton, A. Tarditi, M. S. Chu and the NIMROD Team, "Nonlinear magnetohydrodynamics simulation using high-order finite elements," Journal of Computational Physics **195**, 355 (2004).

[8] B. N. Rogers and J. F. Drake, "Diamagnetic stabilization of ideal ballooning modes in the edge pedestal," Physics of Plasmas **6**, 2797 (1999).

[9] C. R. Sovinec, T. A. Gianakon, E. D. Held, S. E. Kruger, D. D. Schnack, and the NIMROD Team, "NIMROD: A computational laboratory for studying nonlinear fusion magnetohydrodynamics," Physics of Plasmas **10**, 1727 (2003).

[10] For example, N. A. Krall and A. W. Trivelpiece, *Principles of Plasma Physics* (McGraw-Hill, 1973).

[11] L. Spitzer, Jr., *Physics of Fully Ionized Gases* (Interscience Publishers Inc., New York, 1956).

[12] D. P. Brennan, E. D. Held, S. E. Kruger, A. Y. Pankin, D. D. Schnack, and C. R. Sovinec, "Final report for the OFES ELM milestone for FY2005," GA-A25229, UW-CPTC 05-8 (September 30, 2005).

[13] S. I. Braginskii, "Transport Processes in a Plasma," *Reviews of Plasma Physics*, Vol. 1, 205 (Consultants Bureau, New York, 1965).

[14] Phillip Snyder, private communication.

[15] K. V. Roberts and J. B. Taylor, "Magnetohydrodynamic Equations for Finite Larmor Radius," Physical Review Letters **8**, 197 (1962).

[16] R. J. Hastie, P. J. Catto, and J. J. Ramos, "Effect of strong radial variation of the ion diamagnetic frequency on internal ballooning modes," Physics of Plasmas **7**, 4561 (2000).

[17] C. R. Sovinec, D. D. Schnack, A. Y. Pankin, D. P. Brennan, H. Tian, D. C. Barnes, S. E.

Kruger, E. D. Held, C. C. Kim, X. S. Li, D. K. Kaushik, S. C. Jardin, and the NIMROD Team, “Nonlinear Extended Magnetohydrodynamics Simulation Using High-Order Finite Elements,” Journal of Physics: Conference Series **16**, 25 (IoP, London, 2005).

[18] C. R. Sovinec, H. Tian, D. D. Schnack, A. Y. Pankin, and D. C. Barnes, "Semi-Implicit Extended MHD Simulation," presented at the 47th Annual Meeting of the Division of Plasma Physics of the American Physical Society, Denver, Colorado, 2005. Bulletin of the American Physical Society 50, no. 8, paper CP1.77 (October, 2005—poster available from http://www.cptc.wisc.edu/sovinec_research).

[19] D. D. Ryutov, B. I. Cohen, R. H. Cohen, E. B. Hooper, and C. R. Sovinec, “The Effect of Artificial Diffusivity on the Flute Instability,” Physics of Plasmas **12**, 84504 (2005).

[20] X. S. Li and J. W. Demmel, “SuperLU_DIST: A Scalable Distributed-Memory Sparse Direct Solver for Unsymmetric Linear Systems,” ACM Transactions on Mathematical Software, **29**, 110 (2003).

[21] J. A. Holmes, B. A. Carreras, P. H. Diamond, and V. E. Lynch, “Nonlinear dynamics of tearing modes in the reversed field pinch,” Physics of Fluids **31**, 1166 (1988). Y. L. Ho and G. G. Craddock, “Nonlinear dynamics of field maintenance and quasiperiodic relaxation in reversed-field pinches,” Physics of Fluids B **3**, 721 (1991).

[22] Y. Saad and M. Schultz, "GMRES: A Generalized Minimal Residual Algorithm for Solving Nonsymmetric Linear Systems." SIAM Journal on Scientific and Statistical Computing **7**, 856 (1986).

[23] W. Park, E. Belova, G. Fu, et al, Phys Plasmas 6, 1796 (1999)